


Research Article

Microbial degradation of Pleistocene permafrost-sealed fossil mammal remains

Gabriela Calábková^{a,b}, Jiří Chlachula^{c,d*} , Martin Ivanov^a, Michaela Hložková^e, Jolanta Czerniawska^c, Michaela Vašínová-Galiová^{f,g}, Lubomír Prokeš^{e,h} and Petr Gadas^a

^aDepartment of Geological Sciences, Faculty of Science, Masaryk University, Brno, Czech Republic; ^bDepartment of Geology and Paleontology, Moravian Museum, Brno, Czech Republic; ^cInstitute of Geocology and Geoinformation, Faculty of Geographical and Geological Sciences, Adam Mickiewicz University, Poznan, Poland; ^dEnvironmental Research Centre, Stare Mesto, Czech Republic; ^eDepartment of Chemistry, Faculty of Science, Masaryk University, Brno, Czech Republic; ^fInstitute of Chemistry and Technology of Environmental Protection, Faculty of Chemistry, Brno University of Technology, Brno, Czech Republic; ^gBIC Brno, Czech Republic and ^hDepartment of Physics, Chemistry and Vocational Education, Faculty of Education, Masaryk University, Brno, Czech Republic

Abstract

Paleontological remains retrieved from permafrost represent the most informative records of Pleistocene ecosystems. Different levels of past microbial activity affecting fossil material preservation are presented for two selected bone samples—an almost intact *Bison* sp. metacarpus (45.0 ± 5.0 ^{14}C ka BP) and a weathered *Equus* sp. metacarpus (37.8 ± 1.7 ^{14}C ka BP) from the recently exposed cryogenic geo-contexts in the Yana River basin, NE Yakutia. Diagenetic changes in bone porosity and chemical composition as a result of the past microbial activity were investigated by multiple analytical methods. In the bison bone, which was permafrost-sealed shortly after death of the animal and conserved for ca. 45 ka in a frozen state in a cryolithic formation, only superficial microbial degradation processes were detected. Progressive microbial attacks characterize the horse bone, which was exposed to MIS 3 sub-aerial biogenic decay and modern surficial weathering. This is evidenced by extensive bacterial micro-boring with the typical focal destructions, an increase in microbial porosity, and de-mineralized osseous zones due to waterlogged and poorly oxygenated past depositional conditions. New information contributes to better understanding of the diagenesis particularities and the associated chemical and biological agents of the fossil osteological assemblages with respect to their taphonomic and paleoenvironmental implications.

Keywords: Pleistocene, Yakutia, Yana Basin, Batagay thermokarst sinkhole, Permafrost, Fossil osteological material, Diagenesis, MIS 3 environment, Fauna remains preservation

(Received 29 August 2021; accepted 16 May 2022)

INTRODUCTION

Fossil bones and teeth represent significant sources of proxy information on past environments, the geographic mobility and paleodiet of the Pleistocene animals, and post-depositional taphonomic processes. The present climate warming observed in NE Siberia with annual air temperature rise by up to $+3^\circ\text{C}$ during the last four decades (Danilov and Degteva, 2018; Czerniawska and Chlachula, 2020) has triggered exposures of Pleistocene-age geological sections sealing rich fossil fauna records (e.g., Plotnikov et al., 2016; Kirillova et al., 2020; Chlachula et al., 2021), some in a unique state of preservation (Boeskorov, 2009; Boeskorov et al., 2013; Chernova et al., 2015). Bones are exposed to a variety of factors during the fossilization processes that are reflected in the changes of original chemical composition and micromorphology of the bone tissue formed by two principal components: collagen and calcium phosphate. During the early

stages of diagenesis, micro-organisms (e.g., bacteria, fungi, cyanobacteria) have a crucial effect on bone preservation because of their expansion into the bone tissue immediately after the animal's death. Microbial activity is strongly affected by the specific ambient conditions of the microorganisms that are required for their growth and reproduction (Bell et al., 1996, Trueman and Martill, 2002, Turner-Walker, 2012). Traces of the microbial activity captured within the bone microstructure provide a unique opportunity to investigate past depositional (burial) environments and reconstruct long-term conditions for fossil material preservation.

A detailed study of microbial attacks (Hackett, 1981) resulted in differentiation of two main categories of microbial bio-erosion. The first category of microbial attacks created by bacteria, microscopic focal destruction (MFD), is characterized by a poriferous structure with pores 0.1–1 μm in diameter (spongiform porosity) (Jacks et al., 2001, Turner-Walker et al., 2002) and the presence of hyper-mineralized rims of amorphous bioapatite (Jans et al., 2004, Jans, 2008). The MFDs are divided into three sub-groups based on the shape and the extension within the bone tissue conditioned by different tissue types: (1) linear longitudinal, which is usually circular with the smallest foci (LLF) 5–10 μm in diameter; (2) budded, which are more irregular (a shape similar to a bud)

*Corresponding author email address: <paleo@amu.edu.pl>

Cite this article: Calábková G, Chlachula J, Ivanov M, Hložková M, Czerniawska J, Vašínová-Galiová M, Prokeš L, Gadas P (2023). Microbial degradation of Pleistocene permafrost-sealed fossil mammal remains. *Quaternary Research* 111, 84–106. <https://doi.org/10.1017/qua.2022.28>

with the larger foci (BF) 30–60 µm in diameter; and (3) lamellate, which is the least common foci (LF) 10–60 µm in diameter, reflecting the lamellar structure of the bone tissue, and are the only ones can pass through the cement line. The budded and lamellate foci can exceptionally reach up to 250 µm in diameter and both have granulous infill (Hackett, 1981, Jans et al., 2004). The second category of microbial attacks, called “Wedl tunneling,” displays empty tunnels 5–15 µm in diameter with sharp and well-calcified walls (Marchiafava et al., 1974; Hackett, 1981; Jans, 2008; Turner-Walker and Jans, 2008) that are often attributed to the activity of aquatic organisms such as fungi (Wedl, 1864; Marchiafava et al., 1974), algae (Davis, 1997; Fernández-Jalvo et al., 2010; Nacarino-Meneses et al., 2021), and cyanobacteria (Davis, 1997; Turner-Walker and Jans, 2008).

Bacteria are the most varied microorganisms living within a broad range of diverse environments. They are adapted to specific temperatures, pH values, oxygen, or soil contents. Aerobic soil bacteria are mostly involved in post-mortem changes in the bone microstructure and contribute preferably to the deterioration of the cortical bone tissue near the periosteal and endosteal surface (Turner-Walker, 2008, 2012, 2019; Turner-Walker and Jans, 2008, Fernández-Jalvo et al., 2010; Müller et al., 2011; Fernández-Jalvo and Andrews, 2016; Kendall et al., 2018). Nevertheless, in several studies, great importance in bone degradation has been given to intestinal bacteria (Bell et al., 1996; Jans, 2008; White and Booth, 2014), although this has never been clearly proven. Bacterial activity also may induce the process of biomineralization, especially in the form of iron- or manganese-bearing minerals, such as oxides and hydroxides (Mandernack et al., 1995a, b; Kremer et al., 2012), phosphates (Turner-Walker, 2012), or iron sulphides created by sulphate-reducing bacteria (Turner-Walker, 1998).

Apart from the microbial activity, other physical, (geo-) chemical, and biological factors jointly affect fossil osteological material causing mineral content instability. Carbonate apatite $[\text{Ca}_{10-a}(\text{PO}_4)_{6-b}(\text{CO}_3)_c(\text{OH})_{2-d}]$, which is the principal bone constituent chemically similar to hydroxyapatite $[\text{Ca}_5(\text{PO}_4)_3(\text{OH})]$, and other chemical components are not resistant to postmortem mineralogical enrichment or depletion (Berna et al., 2004; Kremer et al., 2012; Reynard and Balter, 2014; Keenan and Engel, 2017). A combination of techniques is applied to characterize the bones or teeth chemical element composition and the state of diagenesis (Goodwin et al., 2007; Piga et al., 2009; Galiova et al., 2010; Lebon et al., 2010; Swanston et al., 2012; Liao et al., 2019). Quantification of the diagenetic changes and their visualization is usually performed by laser ablation-inductively coupled plasma-mass spectrometry (LA-ICP-MS).

This study presents results on varying bio-degradation of the Late Pleistocene (MIS 3) megafauna skeletal remains sealed in fossil permafrost. A marked discrepancy of microbial activity controlling bone preservation is documented on the example of an intact and perfectly preserved bison metacarpus and a weathered horse metacarpus. The analyses point to specific taphonomic histories predetermining the diagenetic processes and differential bone matrix preservation. The results add to our understanding of the contextual particularities of osteological material decay and the associated chemical and biological agents that affect the state of preservation of paleontological assemblages.

Study Area

The study area is located in the central and northern part of the Verkhoyansk Region, NE Yakutia (Fig. 1), within a low-relief zone

characterizing the middle reaches of the Yana River basin. The sub-Arctic climate at the northern limits of the boreal forest is very harsh, sub-continental, with extreme seasonality. Mean annual air temperature (MAAT) in the central part of the basin (Batagay) is -15°C (average January temperature -45.2°C , average July temperature $+16.2^\circ\text{C}$), 50–70 days per year are frost-free, the mean annual precipitation is 200–300 mm (Agroclimate Database, 1963; Bulygina and Razuvaev, 2012). Continuous permafrost, reaching up to 300 m in depth, underlies the broader territory (Harada et al., 2006; Grosse et al., 2013; Fedorov et al., 2018).

During the last glacial maximum (LGM), summer temperature was $\sim 6\text{--}8^\circ\text{C}$ lower and winter temperature $\sim 12\text{--}14^\circ\text{C}$ lower than the present (Frenzel, 1962; Velichko, 1993). Progressive warming and ground surface heat absorption observed across Yakutia have triggered changes in the local hydrology systems, mass gravity-flow processes, thermokarst formation, and frozen-ground thaw (Duchkov, 2006; Popp et al., 2006; Iijma et al., 2010; Romanovsky et al., 2010; Malkova et al., 2011; Veremeeva and Glushkova, 2013; Fedorov et al., 2014; Schuur et al., 2015; Czerniawska and Chlachula, 2020). The northern lowlands are seasonally water-saturated and boggy as a result of accelerated river-flow dynamics due to the progressing late spring–early summer permafrost thaw. Associated channel erosion and bank undercutting expose the pre-modern (late Pleistocene–early Holocene) organic-rich grounds with embedded fossil fauna and macrofloral remains (Chlachula et al., 2014). The northern boreal forest of larch (*Larix sibirica*), transgressing into tundra-forest in the upper elevations, is the principal biotope in the lowlands and adjoining mountain foothills (Andreev et al., 2001).

The geologically youngest formations that are the subject of investigations related to the mid-last glacial (MIS 3/Karga) interstadial (55–24 ka BP). This time interval is associated with the principal late Pleistocene paleontological and early cultural occurrences in the Yana-Indigirka-Kolyma lowlands that are buried in fossiliferous sandy, gravelly alluvial and silty, clayey lacustrine facies (Biske, 1957; Boeskorov, 2005, 2010; Lazarev, 2008; Lazarev et al., 2011; Cheprasov et al., 2015; Chlachula et al., 2021). During the early part of the interstadial (55–38 ka BP), the central and upper Yana River valley was covered by parkland-steppes and mixed taiga forests that supported populations of large herbivorous animals (mainly mammoth, woolly rhinoceros, bison, and horse), as evidenced by the rich osteological records and fossil mammal coprolites retrieved from the cryolithic formations (Chlachula et al., 2014, unpub.). Fossil herbaceous plants ($\sim 70\text{--}80\%$) with sporadic arboreal taxa of *Larix*, *Betula*, *Alnus*, and *Salix* point to relatively warm conditions (Murton et al., 2017; Ashastina et al., 2018). Overall, the Karga Interstadial was biotically the most productive mid-last glacial stage, with rich paleontological sites distributed across Yakutia (e.g., Boeskorov, 2010; Boeskorov et al., 2013; Plotnikov et al., 2016).

The Yana River Basin (YRB Site)

The first investigated site (YRB/Yunigen) is located in the middle reaches of the Yana River ($68^\circ 54' 20.78''\text{N}$, $134^\circ 26' 42.75''\text{E}$, 85 m asl.), ~ 250 km downstream of the Batagay Site (BAS) (Fig. 1). Contextually, the YRB site is geologically structured by ancient colluvia overlying a laterally eroded gravelly terrace platform exposed 20–30 m above the present river channel. There, as well as at other loci in the nearby area, abundant osteological remains of Pleistocene ungulates (mammoth, rhinoceros, bison, horse, and reindeer, among others), along with large carnivores (bear, lion,



Figure 1. Location map of the study area with the investigated sites.

hyena, wolf), are found in intact positions or partly re-deposited in frozen strata. These sandy gravel and sandy/silty clay formations are exposed due to permafrost thaw and/or water pumping (Chlachula et al., 2014). The analyzed osseous material originates from the upper part of the documented stratigraphic section (Fig. 2A).

The YRB/Yunigen site is one of the key paleoenvironmental reference sites for chronostratigraphic correlations and paleoecological interpretations of the mid-last glacial ecosystems and early human (Paleolithic) occupation in the (sub-)Arctic East Siberia.

The Batagay Thermokarst Sinkhole (BAS Site)

The second paleontological site ($67^{\circ}34'55.9''\text{N}$, $134^{\circ}45'55.8''\text{E}$; 241 m asl/top surface) lies near the confluence of the Yana and Adycha rivers at the southern margin of a major thermokarst sinkhole/cryolithic crater (the Batagay “proval”), 15 km SE of Batagay town (the Verkhoyanskiy District) (Fig. 1). The geomorphic setting represents the most spectacular place of active permafrost-degradation processes in Siberia (Kunitsky et al., 2013). The Batagay depression, reaching the present size of $\sim 800 \times 500$ m and a depth of ~ 60 – 90 m with a lateral face retreat of 10–20 m/year, demonstrates the intensity and the scale of the current frozen ground thaw in the Siberian North due to the dramatic warming trend observed in Yakutia over the past 40 years (Fedorov et al., 2018; Chlachula and Czerniawska, 2021).

The vertical sinkhole is transgressing in the upper part into a conically ($\sim 45^{\circ}$) shaped outer margin. On the eastern side of the

depression, erosion has exposed a complete suite of geological units formed by dark gray silts and laminated fine-grained sands with a slightly wavy structure in the lower and middle part of the sequence. These alluvial/colluvial deposits are overlain by well-sorted aeolian sands. The conformably sequenced sedimentary series represents ancient (Middle–Late Pleistocene) Yana River shallow-water paleochannel deposits and colluvia. Several fossil soils in the middle and upper part of the sinkhole (Fig. 2B) point to stages of the ancient surface stabilization and pedogenesis. Numerous erosion-exposed remains of Pleistocene flora and fauna are found in isolated positions and in discrete humus-rich layers aligned by ice lenses (Chlachula et al., 2014; Ashastina et al., 2018; Opel et al., 2019). Preservation of the incorporated paleontological remains is excellent (Lazarev et al., 2011). The fossil records are the subjects of current contextual taphonomic studies.

AIMS, MATERIAL, AND METHODS

The aim of the study was to define the specific agents affecting differential bone structure degradation and assess the causes of diagenetic changes (chemical and biological) in the analyzed fossil fauna remains. These remains include a bison metacarpus (the YRB site) and a horse metacarpus (the BAS site) that were removed from the Late Pleistocene (MIS 3) permafrost along with other fossils in August 2014 (J. Chlachula). Taphonomic investigations at both sites were performed.

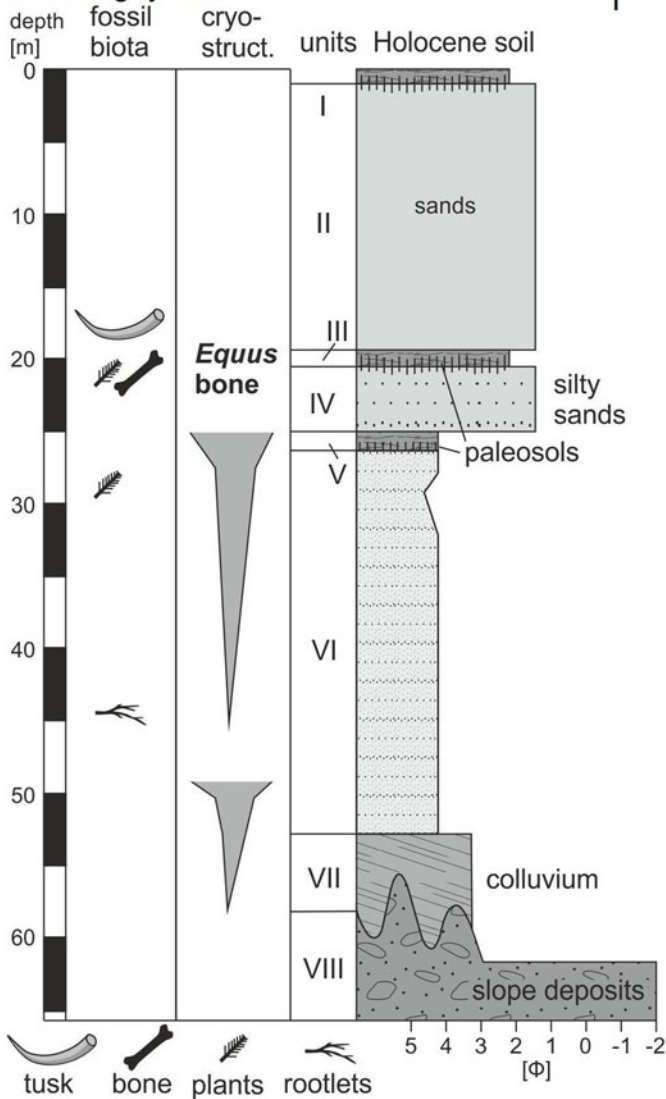
A Yana River Site 1



2



B Batagay Site 1



2



3



Figure 2. Views of the sample study sites. (A) Yana River Site; 1 = cryolithic exposure of the Late Pleistocene fossiliferous formation; 2 = the investigated section; (B) Batagay Site and the Batagay thermokarst sinkhole stratigraphy; 1 = composite site stratigraphy; 2 = thermokarst sinkhole, eastern wall; 3 = the *Equus* bone, SE section. Photographs by J. Chlachula, August 2014.



Figure 3. Analyzed bones. (A) The metacarpus of *Bison* sp.; (B) the metacarpus of *Equus* sp.

Field studies

The first, well-preserved bison (*Bison* sp.) right metacarpal bone (Fig. 3A) was collected in situ directly from a buried permafrost ground (Unit 4) of the YRB site underlain by a solid ice body after exposure of the section by water pumping. The isolated bone was fresh in condition, yellow-white colored, with no macroscopic signs of microbial decay, post-mortem mechanical damage, or Pleistocene carnivore scavenging (e.g., tooth marks). The fused epiphyses indicate an adult animal. The radiocarbon age determination of the sample is $45,000 \pm 5000$ yr BP (Poz-97051).

The second sample represents a partly weathered right *Equus* sp. metacarpus (Fig. 3B) released from the Batagay permafrost sinkhole (the BAS site) as a result of seasonal melting of the massive Pleistocene cryogenic formation. The bone, which was found ~ 30 m from the sinkhole's vertical wall, presumably was exposed on the present surface at the bottom of the crater for some time (2–5 years) prior to sample collection, as deduced from the rate of lateral wall retreat of the thermokarst crater (10–20 m per year; Kunitsky et al., 2013). The radiocarbon age of the bone, $37,800 \pm 1700$ yr BP (Poz-97053), corroborates the ^{14}C date of $36,300 \pm 700$ yr BP (Poz-75782) on fossil roots from the same section (Murton et al., 2017). Both dates confirm the mid-last glacial (MIS 3) age of the upper part of the Batagay stratigraphic sequence (Vasil'chuk and Vasil'chuk, 2019). With respect to the site chronostratigraphy, the initial position of the fossil was likely at ~ 20 m depth below the present top surface and originally sealed within the sedimentary bed (Unit 4) of massive interbedded colluvial sands (Fig. 2B) (the basal part of Unit 5; Murton et al., 2017). The thinner palmar side of the fossil was covered by silty sediments, whereas the thicker dorsal side was exposed and subjected to the extreme, seasonally fluctuating

temperature conditions. The distal epiphysis indicates an adult individual.

Both samples were wrapped up in plastic bags and preserved in a frozen state prior to their air transport to the laboratory of the Department of Geological Science at the Masaryk University in Brno, Czech Republic, for analytical processing.

Laboratory studies

Laboratory studies focused on assessing intensity of the past/present microbial activity in the analyzed fossil records as a study case from the (sub)arctic zone of Northeast Siberia exposed to the current climate warming. Both samples were studied by a combination of several analytical methods including scanning electron microscope analysis (SEM-BSE), electron microprobe analysis (EMPA), laser ablation inductively coupled plasma-mass spectrometry (LA-ICP-MS), and mercury intrusion porosimetry (HgIP).

Sample preparation

The diaphyses of the bison and horse metacarpal bones were cross-cut into slices 1 cm thick. The metaphyseal and epiphyseal parts, where the cortical bone is rather thin or absent, were excluded from the analyses. The slices retaining the thick cortical bone were cut radially (*Bison*: $\sim 1.2 \times 0.8 \times 0.5$ cm; *Equus*: $\sim 1.2 \times 0.8 \times 0.5$ cm [dorsal side], and $\sim 1.0 \times 0.5 \times 0.5$ cm [palmar side]) and leached in acetone for 24 hours to remove fat residues. Subsequently, the samples were dried in an automatic desiccator at 40°C for 48 hours. The prepared samples were used for the BSE-SEM and HgIP studies, with the former vacuum-coated with gold.

EMPA and LA-ICP-MS analyses were performed on a polished block section of the bone slice embedded in epoxy resin (~2.5 cm in diameter). The sample surface was carbon coated for EMP study. The palmar and dorsal bone sides were treated separately.

Scanning electron microscopy (SEM-BSE)

A Jeol JSM-6490LV electron microscope in the Department of Geological Sciences, Masaryk University, Brno (MU Brno), was used for detailing the bone microstructure on the surface as well as cross-section using an accelerating voltage of 15 kV.

Mercury intrusion porosimetry

The AutoPore IV 9500 mercury intrusion porosimetry analysis (Department of Geological Sciences, MU Brno) was applied to assess the overall distribution of pore sizes represented in the horse and bison cortical bone tissue. The porosimetry model operates at a pressure of 414 MPa covering pore diameters within the range of 0.003–360 μm . The pore size distribution followed the classification of Turner-Walker et al. (2002): S- or sub-fibril porosity = pores with a diameter <0.1 μm ; M- porosity induced by microbial activity = pores with a diameter in the range of 0.1–1 μm ; L- physiological and dissolution porosity = pores with a diameter >1 μm .

Electron microprobe analysis

The EMP analysis using a Cameca SX100 electron microprobe (Department of Geological Sciences, MU Brno) detailed the chemical composition of the cross-sections through the horse and bison cortical bone tissue (from the periosteal to the endosteal margins, including pore fillings) in the wavelength dispersive mode and an accelerating voltage of 15 kV, beam current of 10 nA and a spot size of 5 μm . Data were processed using the X-Phi matrix correction (Merlet, 1994) and recalculated in the FORMULA program after the values below the detection limit were removed.

Altered apatite was normalized to 12.5 anions and 8 cations according to an idealized formula for hydroxyapatite of $\text{Ca}_5(\text{PO}_4)_3(\text{OH})$. The presence of phosphate with a significant Fe content was proven in some vascular canals, predominantly within the endosteal and periosteal area. Data were converted to the formula of vivianite $\text{Fe}_3(\text{PO}_4)_2 \cdot 8(\text{H}_2\text{O})$ that was normalized to eight cations. The analyzed phosphates contain H_2O either in the form of molecular water (vivianite) or as a hydroxyl anion (apatite). Because the H_2O and carbon contents cannot be determined by routine EMP analysis, they were not included in the formula recalculations (Tables 1–3).

Laser ablation-inductively coupled plasma-mass spectrometry (LA-ICP-MS)

LA-ICP-MS analyses were conducted with two different instrumental setups. The laser ablation system Analyte G2 (Teledyne CETAC Technologies, Omaha, USA) was connected to a double-focusing sector field ICP-MS Element 2 (Thermo Fisher Scientific, Bremen, Germany). This system is installed at the Laboratory of Atomic Spectrochemistry (LAS), MU Brno. The other system, located at the University of Technology in Brno, consists of quadrupole based ICP-MS Agilent 7900 (Agilent Technologies, Santa Clara, CA, USA) coupled with the Analyte Excite+ laser ablation system (Teledyne CETAC Technologies, Omaha, USA). Both instruments used the ArF* excimer laser ablation systems operating at 193 nm equipped with a tunable

2-volume ablation cell HelEx II. Ablation was carried out in the He atmosphere. The operating conditions of the ICP mass spectrometers were optimized using NIST SRM 612.

The elemental distributions across the bone samples were investigated by a line of spots using the laser beam spot size of 65 μm and individual spot spacing of 100 μm , fluence of 9 J/cm^2 , frequency of 10 Hz, dwell time of 60 s, and washout of 60 s. Time-resolved signals were recorded for the following isotopes: $^{23}\text{Na}^+$, $^{24}\text{Mg}^+$, $^{27}\text{Al}^+$, $^{28}\text{Si}^+$, $^{31}\text{P}^+$, $^{42}\text{Ca}^+$, $^{43}\text{Ca}^+$, $^{44}\text{Ca}^+$, $^{45}\text{Sc}^+$, $^{47}\text{Ti}^+$, $^{51}\text{V}^+$, $^{53}\text{Cr}^+$, $^{55}\text{Mn}^+$, $^{57}\text{Fe}^+$, $^{63}\text{Cu}^+$, $^{66}\text{Zn}^+$, $^{75}\text{As}^+$, $^{88}\text{Sr}^+$, $^{137}\text{Ba}^+$, and $^{208}\text{Pb}^+$.

2D elemental mapping of the small specific areas (structure of the diagenetically modified phosphate phase, in which a change caused by the microbial activity was exempt) was accomplished by line scanning. The laser spot diameter was 8 μm , scan speed 4 $\mu\text{m}/\text{s}$, fluency 9 J/cm^2 , and frequency 10 Hz. A distance of 15 μm between individual lines was kept constant. Only the selected elements were subjected to the elemental association investigation (matrix: Ca, P; minor: Na, Mg; and trace elements: Mn, Fe, Sr, Ba, Al, Si).

Standard reference materials NIST SRM 1486 bone meal and NIST SRM 610 glass were used for quantification purposes, and Ca was used as an internal reference element. Ca content was determined using an electron microprobe. The limit of detection was calculated as three times the standard deviation of the He-Ar gas blank divided by sensitivity.

The detection limits were as follows: 3 mg/kg Na; 0.08 mg/kg Mg; 0.09 mg/kg Al; 12 mg/kg Si; 0.57 mg/kg P; 19 mg/kg Ca; 0.02 mg/kg Sc; 0.67 mg/kg Ti; 0.01 mg/kg V; 0.19 mg/kg Cr; 0.02 mg/kg Mn; 1.9 mg/kg Fe; 0.05 mg/kg Cu; 0.02 mg/kg Zn; 0.05 mg/kg As; 0.01 mg/kg Sr; 0.04 mg/kg Ba, and 0.04 mg/kg Pb in a case of line of spots (Table 4); and 4.8 mg/kg Na; 21 mg/kg Mg; 8.4 mg/kg Al; 180 mg/kg Si; 19 mg/kg P; 750 mg/kg Ca; 0.9 mg/kg Mn; 90 mg/kg Fe; 0.79 mg/kg Sr; and 0.76 mg/kg Ba when sampling bone tissue via the line scan mode.

LA-ICP-MS is a widespread technique that is applied for qualitative and quantitative elemental distribution in different types of hard tissues (bone, tooth enamel, dentine, and cementum). This method can directly analyze solid samples with spatial resolution down to the μm scale with high sensitivity and low detection limits. Other benefits are isotopic and multi-element analyses and minimum destructiveness.

The LA-ICP-MS analysis was applied only to the horse bone for detailed evaluation of the alteration processes.

RESULTS

Metacarpal samples preservation

The bison metacarpus was completely skeletonized. The bone surface was smooth, without cracks/fissures or flakes (Fig. 3A), which corresponds to weathering stage 1 (Behrensmayer, 1978) applied to periglacial environments (Todisco and Monchot, 2008). There is no surface pattern indicating activity of carnivores/scavengers. The ^{14}C age of the sample corresponds to the time interval of climatically moderate interstadial conditions.

The horse metacarpus, which was exposed on the surface 2–5 years prior to being collected, was less well preserved with a partially damaged distal epiphysis. The bone surface was coarse in places, particularly on the palmar side and towards the epiphyses where a spongy tissue is visible. The dorsal side displays numerous, recently created narrow longitudinal cracks on the

Table 1. Chemical composition of the *Bison* bone carbonate-apatite $\text{Ca}_5(\text{PO}_4)_{2.5}(\text{CO}_3)_{0.5}(\text{OH})$ obtained by electron-microprobe and calculated chemical formulae. wt% = weight percent, b.d.l. = below detection limit; apfu = atoms per formula unit.

analysis No.	1	2	3	4	5	6
SO ₃ wt. %	0.15	b.d.l.	b.d.l.	b.d.l.	b.d.l.	b.d.l.
P ₂ O ₅	28.78	32.36	29.41	33.34	29.54	31.8
SiO ₂	0.08	b.d.l.	b.d.l.	b.d.l.	b.d.l.	b.d.l.
CaO	40.77	43.59	37.59	45.63	39.62	43.24
MnO	0.09	b.d.l.	b.d.l.	b.d.l.	b.d.l.	b.d.l.
MgO	0.55	0.68	0.66	0.72	0.29	0.35
Na ₂ O	0.76	0.63	0.33	0.67	0.41	0.70
BaO	b.d.l.	b.d.l.	0.06	b.d.l.	b.d.l.	b.d.l.
Cl	0.09	0.05	b.d.l.	0.04	0.04	0.03
F	0.47	0.34	0.35	0.41	0.62	0.38
oxides sum	71.74	77.65	68.40	80.81	70.52	76.50
P apfu	2.577	2.693	2.772	2.671	2.714	2.687
Si	0.008	—	—	—	—	—
S ⁶⁺	0.012	—	—	—	—	—
X-site sum	2.597	2.693	2.772	2.671	2.714	2.687
Ca	4.620	4.592	4.484	4.627	4.606	4.623
Mn ²⁺	0.008	—	—	—	—	—
Mg	0.087	0.100	0.110	0.102	0.047	0.052
Ba	—	—	0.003	—	—	—
Na	0.156	0.120	0.071	0.123	0.086	0.135
M-site sum	4.871	4.812	4.668	4.852	4.739	4.810
Cl	0.016	0.008	—	0.006	0.007	0.005
F	0.157	0.106	0.123	0.123	0.213	0.120
Z-site sum	0.173	0.114	0.123	0.129	0.220	0.125
O	12.667	12.861	13.060	12.793	12.854	12.840
cations sum	7.468	7.505	7.440	7.523	7.453	7.497
Anions sum	12.840	12.975	13.183	12.923	13.074	12.965

external bone surface, with moderately developed flaking. This preservation state of horse metacarpus corresponds to weathering stage 2-3 (Todisco and Monchot, 2008). The bone has a dark-colored periosteal and endosteal surface, while the thinner palmar side is completely colored. Increased mobility of humic substances and the presence of Fe-hydroxide coatings on the sealing sand grains and a dark mineral staining (Fig. 3B) point to a periodic ground drying and moistening under a relatively warm to moderate past climatic regime.

Bone micromorphology and microbial bioerosion

Bone degradation is indicated by specific biogenetic changes. In the perfectly preserved bison metacarpus, honeycomb-like pits were observed on the periosteal and endosteal surface in various

extents (Fig. 4A–D), most often close to vascular supply (Fig. 4E). Some of these structures contained smaller pores ~1 µm in diameter (Fig. 4F).

In the horse metacarpus, both biotic and abiotic destructive factors that affected the degree of bone preservation have been revealed inside the bone structure. The SEM analysis provided evidence of extensive bacterial bio-erosion on the periosteal and endosteal surface, where the meandering or variously branched channels consisting of small micro-tunnels 0.3–1 µm in diameter were observed (Fig. 5A).

Typical bacterial microscopic scale destruction was observed on the cross-section of the cortical bone (*Equus*), predominantly in the sub-endosteal and less frequently in the sub-periosteal area. The linear longitudinal (LLF) and budded (BF) foci were detected

Table 2. Chemical composition of the *Equus* bone carbonate-apatite $\text{Ca}_5(\text{PO}_4)_{2.5}(\text{CO}_3)_{0.5}(\text{OH})$ obtained by electron-microprobe and calculated chemical formulae. wt% = weight percent, b.d.l. = below detection limit; apfu = atoms per formula unit.

Analysis No.	1	2	3	4	5	6	7	8	9	10	11	12	13	14	15
SO ₃ wt.%	0.3	0.29	0.33	0.26	0.28	0.33	0.19	0.26	0.27	0.25	0.32	0.22	0.26	0.21	0.24
P ₂ O ₅	30	28.06	30.9	30.18	29.1	28.34	30.18	32.76	30.66	31.87	31.79	29.04	27.98	30.03	31.65
SiO ₂	—	3.91	0.11	—	—	0.39	0.18	0.18	0.21	0.24	0.16	—	0.1	0.11	0.1
CaO	38.5	34.9	39.16	37.44	35.65	35.44	38.33	38.34	37.66	36.53	38.03	38.95	37.99	41.92	41.61
FeO	4.25	4.18	3.55	3.43	4.2	3.24	3.18	3.1	2.84	1.97	1.94	3.04	2.18	1.06	1.09
MnO	0.26	0.3	0.26	3.63	0.33	4.56	1.72	0.51	0.64	0.29	0.49	0.7	0.38	0.2	0.14
MgO	0.16	0.19	0.17	0.23	0.23	0.2	0.19	0.2	0.2	0.24	0.22	0.21	0.12	0.22	0.2
K ₂ O	—	—	—	0.08	—	0.08	—	—	—	—	—	—	—	—	—
Na ₂ O	0.43	0.49	0.41	0.42	0.41	0.49	0.56	0.51	0.61	0.68	0.54	0.43	0.58	0.51	0.48
Cl	0.04	—	0.03	0.03	—	0.03	—	—	0.04	—	—	—	—	—	—
F	0.82	0.69	0.66	0.59	0.48	0.32	0.31	0.45	0.28	0.35	0.52	0.24	0.36	0.3	0.32
oxides sum	74.41	72.72	75.3	76.03	70.48	73.28	74.71	76.12	73.28	72.27	73.79	72.73	69.8	74.47	75.7
P apfu	2.755	2.803	2.831	2.7	2.856	2.614	2.744	3.055	2.9	3.159	3.047	2.671	2.683	2.688	2.86
Si	—	0.461	0.012	—	—	0.042	0.019	0.02	0.023	0.028	0.018	—	0.011	0.012	0.011
S ⁶⁺	0.024	0.026	0.027	0.021	0.024	0.027	0.015	0.021	0.023	0.022	0.027	0.018	0.022	0.017	0.019
X-site sum	2.779	3.29	2.87	2.721	2.88	2.683	2.778	3.096	2.946	3.209	3.092	2.689	2.716	2.717	2.89
Ca	4.474	4.412	4.541	4.239	4.428	4.137	4.411	4.525	4.509	4.582	4.614	4.535	4.609	4.749	4.759
Fe ²⁺	0.386	0.412	0.321	0.303	0.407	0.295	0.286	0.286	0.265	0.193	0.184	0.276	0.206	0.094	0.097
Mn ²⁺	0.024	0.03	0.024	0.325	0.032	0.421	0.156	0.048	0.061	0.029	0.047	0.064	0.036	0.018	0.013
Mg	0.026	0.033	0.027	0.036	0.04	0.032	0.03	0.033	0.033	0.042	0.037	0.034	0.02	0.035	0.032
K	—	—	—	0.011	—	0.011	—	—	—	—	—	—	—	—	—
Na	0.09	0.112	0.086	0.086	0.092	0.104	0.117	0.109	0.132	0.154	0.119	0.091	0.127	0.105	0.099
M-site sum	5	4.999	4.999	5	4.999	5	5	5.001	5	5	5.001	5	4.998	5.001	5
Cl	0.007	—	0.006	0.005	—	0.006	—	—	0.008	—	—	—	—	0.009	—
F	0.281	0.257	0.226	0.197	0.176	0.11	0.105	0.157	0.099	0.13	0.186	0.082	0.129	0.1	0.108
Z-site sum	0.288	0.257	0.232	0.202	0.176	0.116	0.105	0.157	0.107	0.13	0.186	0.082	0.129	0.109	0.108
O	11.771	12.822	12.024	11.662	12.08	11.586	11.834	12.609	12.246	12.877	12.584	11.646	11.667	11.687	12.126

(Continued)

Table 2. (Continued.)

Analysis No.	1	2	3	4	5	6	7	8	9	10	11	12	13	14	15
cations sum	7.779	8.29	7.87	7.721	7.881	7.683	7.779	8.096	7.946	8.209	8.093	7.689	7.716	7.716	7.89
anions sum	12.059	13.08	12.256	11.865	12.256	11.701	11.939	12.766	12.353	13.007	12.77	11.728	11.796	11.796	12.234
Analysis No.	16	17	18	19	20	21	22	23	24	25	26	27	28	29	30
SO ₃ wt. %	0.26	0.24	0.27	0.27	0.19	0.25	0.3	0.29	0.27	0.19	0.25	0.33	0.21	0.24	0.26
P ₂ O ₅	30.13	30.77	30.81	31.35	29.86	29.79	29.25	30.04	29.04	30.53	30.13	31.08	28.41	29.96	30.23
SiO ₂	—	0.16	—	0.07	0.09	—	0.12	—	—	—	—	0.08	0.13	—	—
CaO	37.59	40.84	40.56	36.55	38.95	42.7	38.5	37.34	42.15	39.74	37.52	41.49	34.49	37.33	38.43
FeO	0.25	0.55	0.35	0.23	0.15	0.37	0.27	0.21	0.33	0.69	0.79	1.04	1.3	1.55	1.85
MnO	0.09	0.09	—	—	—	—	—	—	0.1	—	0.2	0.1	0.39	0.34	0.48
MgO	0.2	0.22	0.19	0.3	0.32	—	0.21	0.2	0.23	0.16	0.16	0.15	0.15	0.19	0.23
K ₂ O	—	—	—	—	—	—	—	—	—	—	—	—	—	—	—
Na ₂ O	0.77	0.5	0.48	0.69	0.6	0.48	0.56	0.64	0.58	0.52	0.5	0.51	0.48	0.56	0.59
Cl	—	—	—	—	0.03	—	—	—	—	—	—	—	—	—	—
F	0.49	0.33	0.38	0.52	0.42	0.47	0.24	0.33	0.37	0.47	—	0.35	0.24	0.34	0.22
oxides sum	69.57	73.56	72.88	69.76	70.43	73.86	69.35	68.91	72.91	72.1	69.55	74.98	65.7	70.37	72.2
<i>P apfu</i>	3.011	2.857	2.901	3.226	2.906	2.684	2.888	3.048	2.616	2.91	3.02	2.822	3.043	2.953	2.868
Si	—	0.018	—	0.009	0.01	—	0.014	—	—	—	—	0.009	0.016	—	—
S ⁶⁺	0.023	0.02	0.023	0.025	0.016	0.02	0.026	0.026	0.022	0.016	0.022	0.027	0.02	0.021	0.022
X-site sum	3.034	2.895	2.924	3.26	2.932	2.704	2.928	3.074	2.638	2.926	3.042	2.858	3.079	2.974	2.89
Ca	4.755	4.799	4.832	4.76	4.797	4.868	4.811	4.795	4.805	4.795	4.759	4.768	4.675	4.656	4.614
Fe ²⁺	0.025	0.05	0.033	0.023	0.014	0.033	0.026	0.021	0.029	0.065	0.078	0.093	0.138	0.151	0.173
Mn ²⁺	0.009	0.008	—	—	—	—	—	—	0.009	—	0.02	0.009	0.042	0.034	0.046
Mg	0.035	0.036	0.031	0.054	0.055	—	0.037	0.036	0.036	0.027	0.028	0.024	0.028	0.033	0.038
K	—	—	—	—	—	—	—	—	—	—	—	—	—	—	—
Na	0.176	0.106	0.103	0.163	0.134	0.099	0.127	0.149	0.12	0.114	0.115	0.106	0.118	0.126	—
M-site sum	5	4.999	4.999	5	5	5	5.001	5.001	4.999	5.001	5	5	5.001	5	4.999
Cl	—	—	—	—	0.006	—	—	—	—	—	—	—	—	—	—
F	0.183	0.114	0.134	0.2	0.153	0.158	0.089	0.125	0.125	0.167	—	0.119	0.096	0.125	0.078

(Continued)

Table 2. (Continued.)

Analysis No.	16	17	18	19	20	21	22	23	24	25	26	27	28	29	30
Z-site sum	0.183	0.114	0.134	0.2	0.159	0.158	0.089	0.125	0.125	0.167	—	0.119	0.096	0.125	0.078
O	12.418	12.126	12.2	12.974	12.188	11.64	12.219	12.561	11.483	12.184	12.558	12.039	12.592	12.319	12.133
cations sum	8.035	7.894	7.923	8.259	7.933	7.704	7.928	8.074	7.638	7.927	8.042	7.857	8.079	7.974	7.89
anions sum	12.601	12.241	12.334	13.174	12.347	11.798	12.307	12.686	11.607	12.351	12.558	12.158	12.688	12.444	12.211
Analysis No.	31	32	33	34	35	36	37	38	39	40	41	42	43	44	45
SO ₃ wt. %	0.26	0.28	0.28	0.21	0.24	0.14	0.27	0.2	0.24	0.23	0.25	0.2	0.19	0.24	0.29
P ₂ O ₅	30.37	29.52	29.58	29.52	32.23	27.98	27.07	27.97	26.69	28.02	27.97	25.99	26.58	29.36	27.58
SiO ₂	0.14	1.2	0.53	0.96	0.25	—	0.07	0.1	0.08	—	—	—	0.35	—	1.28
CaO	38.05	37.02	36.95	35.92	41.02	36.33	34.46	34.38	34.21	35.52	36.19	34.73	35.8	38.43	38.14
FeO	2.36	2.37	2.46	2.47	2.64	3.26	3.93	3.9	1.92	2.19	2.42	1.38	1.4	1.63	1.02
MnO	1.58	2.04	0.23	1	0.2	0.25	0.31	0.57	0.39	0.41	0.39	0.32	0.2	0.16	0.19
MgO	0.15	0.18	0.21	0.24	0.21	0.15	0.22	0.25	0.18	0.22	0.25	0.18	0.27	0.18	0.22
K ₂ O	—	—	—	—	0.09	0.06	—	—	0.07	—	—	—	0.07	—	—
Na ₂ O	0.54	0.51	0.58	0.54	0.74	0.5	0.53	0.55	0.53	0.55	0.59	0.56	0.52	0.58	0.64
Cl	0.04	—	—	—	0.11	0.07	0.05	—	—	—	—	0.03	—	—	—
F	0.31	0.4	0.34	0.52	0.44	0.39	0.36	0.52	0.41	0.43	0.53	0.33	0.38	0.33	0.46
oxides sum	73.66	73.35	71.02	71.16	77.96	68.95	67.11	68.22	64.55	67.39	68.37	63.57	65.6	70.77	69.63
P <i>apfu</i>	2.835	2.8	2.893	2.919	2.831	2.746	2.74	2.818	2.826	2.849	2.776	2.751	2.731	2.82	2.687
Si	0.015	0.134	0.061	0.112	0.026	—	0.008	0.012	—	—	—	—	0.042	—	0.147
S ⁶⁺	0.022	0.024	0.024	0.018	0.019	0.012	0.024	0.018	0.023	0.021	—	0.019	0.017	0.02	0.025
X-site sum	2.872	2.958	2.978	3.049	2.876	2.758	2.772	2.848	2.859	2.87	2.798	2.77	2.79	2.84	2.859
Ca	4.495	4.444	4.574	4.496	4.56	4.512	4.414	4.383	4.585	4.571	4.546	4.653	4.655	4.672	4.703
Fe ²⁺	0.218	0.222	0.238	0.241	0.229	0.316	0.393	0.388	0.201	0.22	0.237	0.144	0.142	0.155	0.098
Mn ²⁺	0.148	0.194	0.023	0.099	0.018	0.025	0.031	0.057	0.041	0.042	0.039	0.034	0.021	0.015	0.019
Mg	0.025	0.03	0.036	0.042	0.032	0.026	0.039	0.044	0.034	0.039	0.044	0.034	0.049	0.03	0.038
K	—	—	—	—	0.012	0.009	—	—	0.011	—	—	—	0.011	—	—
Na	0.115	0.111	0.13	0.122	0.149	0.112	0.123	0.127	0.129	0.128	0.134	0.136	0.122	0.128	—
M-site sum	5.001	5.001	5.001	5	5	5	5	4.999	5.001	5	5	5.001	5	5	5.001

(Continued)

Table 2. (Continued.)

Analysis No.	31	32	33	34	35	36	37	38	39	40	41	42	43	44	45
Cl	0.007	—	—	—	0.019	0.014	0.01	—	—	—	—	0.006	—	—	—
F	0.108	0.142	0.124	0.192	0.144	0.143	0.136	0.196	0.162	0.163	0.197	0.13	0.146	0.118	0.167
Z-site sum	0.115	0.142	0.124	0.192	0.163	0.157	0.146	0.196	0.162	0.163	0.197	0.136	0.146	0.118	0.167
O	12.067	12.213	12.301	12.421	12.023	11.762	11.804	11.96	12.002	12.039	11.841	11.798	11.825	11.989	11.932
cations sum	7.872	7.958	7.979	8.05	7.876	7.758	7.772	7.847	7.859	7.87	7.798	7.77	7.791	7.841	7.859
anions sum	12.182	12.354	12.425	12.613	12.187	11.919	11.95	12.156	12.164	12.203	12.038	11.935	11.971	12.107	12.1
Analysis No.	46	47	48	49	50	51	52	53	54	55	56	57	58	59	
SO ₃ wt. %	0.27	0.17	0.19	0.29	0.26	0.2	0.21	0.3	0.25	0.26	0.32	0.22	0.21	0.16	
P ₂ O ₅	26.46	27.75	26.52	27.89	27.26	27.16	26.77	27.31	27.74	27.92	27.61	26.53	26.5	26.48	
SiO ₂	0.29	—	0.08	—	—	0.07	—	—	—	0.09	0.1	—	—	—	
CaO	36.57	38.09	36.94	38.86	38.01	36.86	36.68	36.7	36.38	36.58	36.23	35.25	36.41	34.11	
FeO	0.94	0.42	0.43	0.75	0.82	1.19	1.47	1.91	2.16	1.89	2.39	2.48	1.9	3.68	
MnO	0.32	0.12	0.1	0.1	0.1	0.15	0.14	0.21	0.3	1.56	0.21	0.19	0.12	0.11	
MgO	0.15	0.19	0.23	0.21	0.2	0.23	0.16	0.22	0.12	0.25	0.15	0.18	0.19	0.16	
K ₂ O	0.05	—	—	—	—	—	—	—	—	—	—	—	—	—	
Na ₂ O	0.36	0.55	0.5	0.46	0.69	0.47	0.47	0.48	0.45	0.5	0.5	0.42	0.56	0.55	
Cl	0.17	—	—	—	0.03	—	—	0.03	—	—	—	—	0.1	0.06	
F	0.85	0.34	0.45	—	0.28	0.34	0.34	0.33	0.36	0.43	0.31	0.46	0.48	0.38	
oxides sum	66.03	67.49	65.25	68.56	67.53	66.53	66.1	67.34	67.61	69.3	67.69	65.54	66.25	65.52	
P <i>apfu</i>	2.717	2.757	2.716	2.711	2.675	2.746	2.711	2.729	2.79	2.721	2.77	2.733	2.666	2.732	
Si	0.035	—	0.01	—	—	0.008	—	—	—	0.01	0.012	—	—	—	
S ⁶⁺	0.025	0.015	0.017	0.025	0.023	0.018	0.019	0.027	0.022	0.022	0.028	0.02	0.019	0.015	
X-site sum	2.777	2.772	2.743	2.736	2.698	2.772	2.73	2.756	2.812	2.753	2.81	2.753	2.685	2.747	
Ca	4.752	4.789	4.788	4.78	4.721	4.716	4.701	4.642	4.63	4.511	4.601	4.596	4.636	4.454	
Fe ²⁺	0.095	0.041	0.043	0.072	0.079	0.119	0.147	0.189	0.215	0.182	0.237	0.252	0.189	0.375	
Mn ²⁺	0.033	0.012	0.01	0.01	0.01	0.015	0.014	0.021	0.03	0.152	0.021	0.02	0.012	0.011	
Mg	0.027	0.033	0.041	0.036	0.035	0.041	0.029	0.039	0.021	0.043	0.027	0.033	0.034	0.029	

(Continued)

Table 2. (Continued.)

Analysis No.	46	47	48	49	50	51	52	53	54	55	56	57	58	59
K	0.008	—	—	—	—	—	—	—	—	—	—	—	—	—
Na	0.085	0.125	0.117	0.102	0.155	0.109	0.109	0.11	0.104	0.112	0.115	0.099	0.129	0.13
M-site sum	5	5	4.999	5	5	5	5	5.001	5	5	5.001	5	5	4.999
Cl	0.035	—	—	—	0.006	—	—	0.006	—	—	—	—	0.02	0.012
F	0.326	0.126	0.172	—	0.103	0.128	0.129	0.123	0.135	0.157	0.116	0.177	0.18	0.146
Z-site sum	0.361	0.126	0.172	—	0.109	0.128	0.129	0.129	0.135	0.157	0.116	0.177	0.2	0.158
O	11.71	11.811	11.716	11.801	11.624	11.817	11.715	11.784	11.922	11.756	11.919	11.756	11.557	11.731
cations sum	7.777	7.772	7.743	7.736	7.698	7.772	7.73	7.756	7.812	7.754	7.811	7.753	7.685	7.747
anions sum	12.071	11.937	11.888	11.801	11.733	11.945	11.844	11.913	12.057	11.913	12.036	11.933	11.758	11.889

Table 3. Chemical composition of the *Equus* bone vivianite $Fe_3(PO_4)_2 \cdot 8(H_2O)$ obtained by electron-microprobe and calculated chemical formulae. wt% = weight percent, b.d.l. = below detection limit; apfu = atoms per formula unit.

Analysis No.	15	18	26	27	41
P_2O_5 wt. %	31.87	32.61	31.55	31.72	32.29
SiO_2	0.10	b.d.l.	b.d.l.	b.d.l.	b.d.l.
CaO	0.65	0.34	0.43	0.71	1.03
FeO_{tot}	44.78	42.30	45.71	44.51	44.10
MnO	2.56	5.11	1.99	2.30	2.70
MgO	b.d.l.	0.09	0.09	0.08	0.21
SrO	b.d.l.	b.d.l.	b.d.l.	b.d.l.	b.d.l.
BaO	b.d.l.	b.d.l.	b.d.l.	b.d.l.	b.d.l.
Na_2O	0.09	b.d.l.	b.d.l.	0.12	0.06
F	b.d.l.	b.d.l.	b.d.l.	b.d.l.	b.d.l.
Cl	b.d.l.	b.d.l.	b.d.l.	0.02	b.d.l.
O=F	—	—	—	—	—
O=Cl	—	—	—	—	—
oxides sum	80.05	80.45	79.77	79.46	80.39
P apfu	1.998	2.022	1.992	2.002	2.007
Si	0.007	—	—	—	—
X-site sum	2.005	2.022	1.992	2.002	2.007
Ca	0.052	0.027	0.034	0.057	0.081
Fe^{2+}	2.773	2.591	2.851	2.775	2.707
Mn^{2+}	0.161	0.317	0.126	0.145	0.168
Mg	—	0.010	0.010	0.009	0.023
Sr	—	—	—	—	—
Ba	—	—	—	—	—
Na	0.013	—	—	0.017	0.009
A-site sums	2.999	2.945	3.021	3.003	2.988
Cl	—	—	—	0.003	—
O	8.000	8.000	8.000	7.997	8.000
anions sums	8.000	8.000	8.000	8.000	8.000
cations sums	5.004	4.967	5.012	5.005	4.994

on the bone cross-section (Fig. 5B–D). Chemical demineralization distinctly prevails in the periosteal area, especially on the palmar side of the bone (Fig. 5E, F). Fillings of the vascular canals consist mainly of the vivianite (Vv) (Fig. 5F).

Pore-size distribution

The well-preserved bison bone displays a complete pore size distribution in cortical tissue almost identical with the pore size distribution in the comparative modern bovine bone sample (Fig. 6A, B). The pore size distribution in native mammalian cortical tissue is given by the canalicular porosity (the smallest pores in the area $\sim 0.1\text{--}0.3 \mu m$), the osteocyte lacunae porosity (pore size

Table 4. Elemental contents in dorsal and palmar bone sample determined by LA-ICP-MS expressed as median and median absolute deviation. Contents are listed in mg/kg. The median was chosen so that it would be feasible to eliminate the presence of cracks or physiological pores filled with resin, sediment, or a minor phase with a different chemical composition compared to the phosphate phase.

Element	PALMAR side	DORSAL side	LOD
Ca	261,000 ± 17,000	274,000 ± 21,000	0.02
P	126,000 ± 2600	12,6700 ± 6300	0.57
Na	3200 ± 110	2970 ± 270	3
Mg	984 ± 57	1010 ± 74	0.08
Sr	730 ± 130	810 ± 190	0.012
Ba	71 ± 18	81 ± 25	0.04
Mn	2400 ± 1300	2500 ± 1900	0.02
Fe	13,300 ± 4900	11,200 ± 7100	1.9
Zn	116 ± 17	131 ± 24	0.02
Al	8.2 ± 4.2	11.7 ± 9.4	0.09
Si	774 ± 58	460 ± 150	12
Sc	0.175 ± 0.010	1.96 ± 0.21	0.02
Ti	86.4 ± 8.2	127.0 ± 8.6	0.7
V	0.047 ± 0.032	0.108 ± 0.086	0.013
Cr	0.91 ± 0.11	0.88 ± 0.26	0.19
Cu	0.26 ± 0.07	0.36 ± 0.26	0.05
As	1.26 ± 0.43	2.36 ± 0.98	0.05
Pb	0.49 ± 0.12	1.05 ± 0.37	0.04

ranges = 2–7 µm), and the physiological porosity (pores >10 µm diameter, which represent vascular canals) (Cowin, 1999; Turner-Walker et al., 2002). However, HgIP has a problem with detecting the porosity of osteocyte lacunae because without sufficiently high pressure, mercury does not penetrate the lacuna and is trapped in the canaliculi, the so-called ink-bottle effect (Turner-Walker et al., 2002).

The bison cortical tissue displays an increased volume of the S-porosity (≤ 0.1 µm) and L-porosity (>7 µm). There is no indication of porosity induced by microbial activity (M) within the range of 0.1–1 µm in the fossil bison metacarpus (Fig. 6B).

The weathered Batagay horse bone showed increased M-porosity (Fig. 6C), with the largest pore volume maximum at pores of ~0.35 µm in diameter (the palmar side and the periosteal area) where extensive demineralized zones were detected (Fig. 6D–F). In the endosteal area, pores of ~0.28 µm in diameter represented a significant peak within M-porosity. Almost the same trend was observed in the endosteal area of the dorsal side.

Chemical composition

The mineral component of the studied bison and horse bone (Tables 1, 2), reflecting the state of diagenesis and osteological preservation, corresponds to the carbonate-apatite content with the ideal formula $\text{Ca}_5(\text{PO}_4)_2.5(\text{CO}_3)_{0.5}(\text{OH})$. This contributes to the bioapatite composition in extant remains, where the actual carbonate content varies among different species and increases with age within a given species (Legros et al., 1987). Mineral re-crystallization into hydroxyapatite results from postmortem

unstable conditions (e.g., Sillen and Parkington, 1996; de Sousa et al., 2020). The deficit in the sum of oxides measured by the EMP analysis could be a result of the porous structure of the bone material and the presence of organic components or carbonates or both. The exogenous elements were incorporated into the structure of apatite in place of the cation/anion position or concentrated inside the physiological pores or cracks.

The analytical study was performed only on the horse metacarpus by the LA-ICP-MS on the palmar (Fig. 7A–D) and dorsal (Fig. 7E–H) sides of the bone (Figs. 7, 8). Distributions of the Ca and P matrix (Fig. 7A, E) and the Na and Mg elements (Fig. 7B, F) show their representation within the sample with some apparent fluctuations on the dorsal bone side. The LA-ICP-MS shows increased concentrations of Mn and Fe (Fig. 7C, G), which are orders of magnitude lower in native bone (Skinner, 2005). It also shows the presence of other exogenous elements, such as Sr, Ba (Fig. 7B, F), and As, Cu, and V (Fig. 7H), incorporated into the bone mineral matrix at the expense of major elements Ca and P (Fig. 7A, E) and minor elements Na and Mg (Fig. 7F). Al and Si were present in a physiological foramen or cracks, which corresponded with the highest peaks in two-spot positions (Fig. 7D).

Bone structure 2D element imaging

2D bone mineralogy mapping was performed in three selected loci of the *Equus* metacarpus (Fig. 8). These loci show concentrations close to the endosteal part of the compact bone where the vascular systems occur. The Ca and P maps indicate homogeneous distributions over the entire area of the analyzed surface except for osteons, pores, and cracks. Alteration of the phosphate phase is apparent from the Na, Mn, and Fe distributions. The different structure around vascular canals is most evident from the change in Na distribution where the area in the vicinity of pores is Na depleted and subsequently is bordered with “rings” having higher Na content (Fig. 8A). The differential distribution of Mn and Fe highlights a distinct structure and an incorporation of elements into the phosphate phase. The presence of Mn may indicate microbial activity.

The secondary mineral phase (Fig. 8A) fills the vascular pores and the nearby cracks, as evident from the distribution of Mn and Fe, and corresponds to the presence of vivianite. The sums of oxides in the analyzed horse bone vivianite captured mainly near the periosteum are ~7% higher compared to the ideal vivianite (73%). This may be due to the presence of Fe or Mn phosphate with a lower H₂O content (Pratesi et al., 2003; Chukanov et al., 2014) (Table 3). Element mapping shows a positive association among P, Fe, Mn, and Mg within the vascular canal, with Mg and Mn incorporated into the vivianite structure.

The distributions of Ca and P, as with the principal matrix elements, are rather uniform across the whole analyzed area, however their content decreases in the vicinities of bone margins, physiological pores, or cracks (Fig. 8B). Secondary microporosity close to the periosteum was filled exclusively with Mn (up to 0.5%_{m/m}; the red area) and Fe (up to 6.0%_{m/m}; the red area), while the surrounding tissue was distinctly Fe saturated (~4.3%_{m/m}; the green area). This porous structure showed the high content of Mn²⁺ ions.

The quantified distributions of Ca, P, Na, Fe, and Mn display very heterogeneous spatial patterns for all of these elements (Fig. 8C). The MFDs near the endosteum show absence of impurities or secondary minerals in contrast with the surrounding bone tissue. In the MFDs, which are characterized by the presence

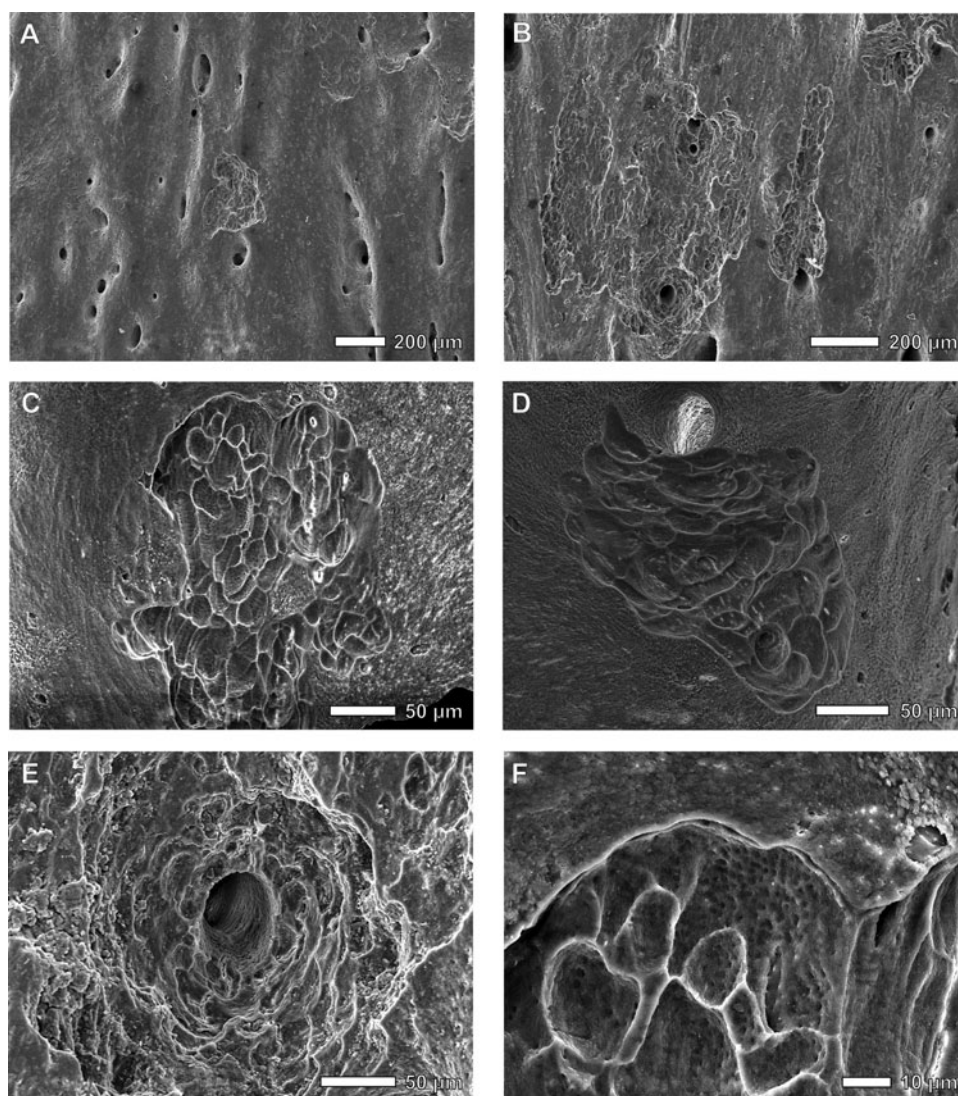


Figure 4. Micromorphology and microbial bioerosion SEM images of the fossil bison bone. (A, B) smooth periosteal surface with the resorption pits; (C, D) isolated honeycomb-shaped resorption pits; (E) resorption pits surrounding vascular canal; (F) detail of pits showing microbial attacks to the *Bison* bone structure.

of a hypermineralized rim that is resistant to leaching, there was also no contamination of exogenous elements.

ENVIRONMENTAL AND TAPHONOMIC IMPLICATIONS OF BONE DECAY

Several diagenetic agents were identified analytically in the studied bison bone (45.0 ± 5.0 ^{14}C ka BP) and horse bone (37.8 ± 1.7 ^{14}C ka BP) from the central Yana River valley and the Batagay thermokarst sinkhole. The rate of decay of mammalian remains in the High Arctic environments (Sutcliffe, 1990) is controlled by (1) the geological context and position of fossils (buried vs. surface-exposed); (2) the amount of ground moisture; (3) pH of the sealing deposits; (4) duration of annual snow cover; and (5) the scale of exposure to atmospheric processes (temperature, precipitation).

The Bison sp. (YRB Site)

The complete skeletonized *Bison* bone (Fig. 3A) displays no traces of transport—only minor surface weathering (WS 1) and lack of

incorporated exogenous elements. This indicates that the bone was not exposed on the surface for a long time after the animal's death when it was buried and subsequently sealed in the gravelly cryolithic deposits. Only superficial resorption pits with a honeycomb pattern (Fig. 4A–F) have been observed in the bone, indicating a short-term effect of microbial activity. A comparable honeycomb pattern is known in the tooth enamel and bones from continental aquatic environments (Fernández-Jalvo and Andrews, 2016). Howship's lacunae, which form during osteoclastic resorption, have a similar shape (Relucanti et al., 2020). Because the microstructures also have been observed on the periosteal surface of the bone, microorganisms such as cyanobacteria or algae appear to be the most likely causal agents.

The bison body decomposition began shortly after death of the animal in a climatically moderate interstadial sub-arctic environment. Under colder conditions, the main soft-tissue decay can take 4–7 days (Janaway et al., 2009). Body skeletonization is significantly accelerated by the activity of insects, other arthropod species, and soil microorganisms (Smith, 1986). Even in periglacial conditions, insect development flourishes within the range of 10–15°C, although many common blow flies cease laying their

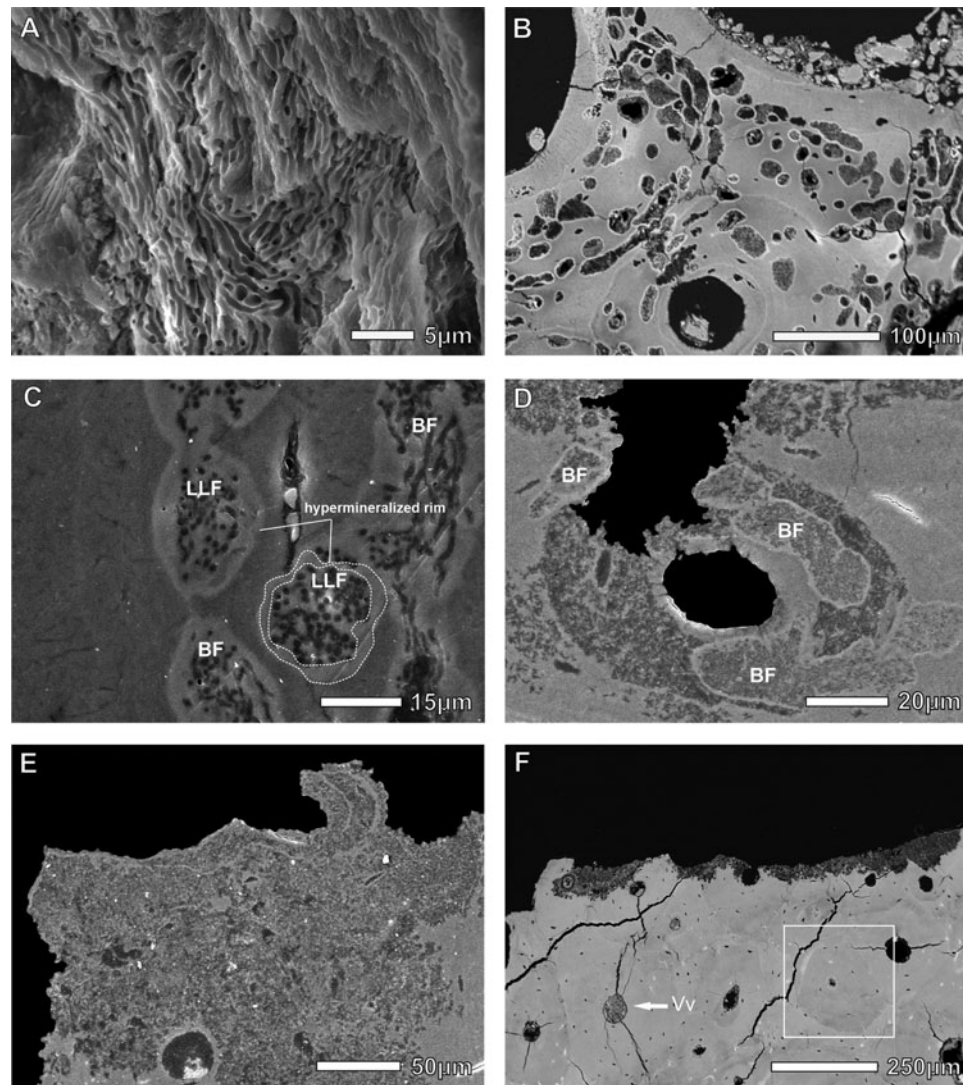


Figure 5. SEM images of the fossil horse bone showing microbial bioerosion. (A) Micro-tunnels created by bacteria on the bone surface; (B) typical microscopic focal destruction (MFD) extended in the endosteal bone area; (C) magnified linear longitudinal (LLF) and budded foci (BF) bounded by hypermineralized rims; (D) bacterial budded foci (BF) overlapping the demineralized zone; (E) magnified bone tissue with signs of advanced demineralization at the periosteal margin; (F) superficially dissolved bone tissue spreading from the periosteal margin with gradually demineralized secondary osteon (white square) and mineral vivianite (Vv) in the vascular canal.

eggs at temperatures below 10°C (Erzinclioğlu, 1996). A maggot (fly larva) can develop completely in ca. 30 days at temperatures ~15°C (Grassberger and Reiter, 2002). Even under cold weather conditions, the temperature for maggot growth can be favorable, depending on the degree of infestation of the carcass (Byrd and Castner, 2010).

During the early stage of the Karga (MIS 3) interstadial (ca. 55–38 ka BP), the MAAT in North Yakutia was close or even higher than today, as indicated by the permafrost-sealed paleoecology records (Chlachula et al., 2021). Especially in summer, insects affected and contributed to accelerated carcass decay of the large roaming fauna. Bacterial reproduction is largely slowed at <12°C, and bacterial growth is substantially inhibited at temperatures <4°C (Binford, 1978; Micozzi, 1997). At temperatures below –5°C, the activity of enzymes and microorganisms is interrupted, and no decomposition occurs (Janaway et al., 2009). Rapid drying of soft tissues due to solar radiation and freezing causes extensive loss of moisture and nutrients from the cadaver,

and most of the carrion fauna ceases bone decomposition (Carter et al., 2007; Smith, 1986). The nearly perfect preservation of the bison bone is primarily due to rapid burial of the bison body/skeleton and long-term preservation in stable cryolithic conditions over the past 45,000 years.

The Equus sp. (BAS Site)

Very low temperatures (average January temperature –51°C based on organic microinclusions in ice-wedges of the Batagay yedoma dated to 33,800–27,100 cal. yr) (Vasil'chuk and Vasil'chuk, 2019) attest to the long-term frozen ground conditions that contributed to the supreme preservation of the fossil remains. The poor preservation of the *Equus* sample (Fig. 3B) provides evidence of much more dynamic environmental conditions. The lower stage of surface abrasion probably caused by wind erosion along with the absence of a chalky external layer indicate that the horse bone was not exposed to external conditions for a long time before

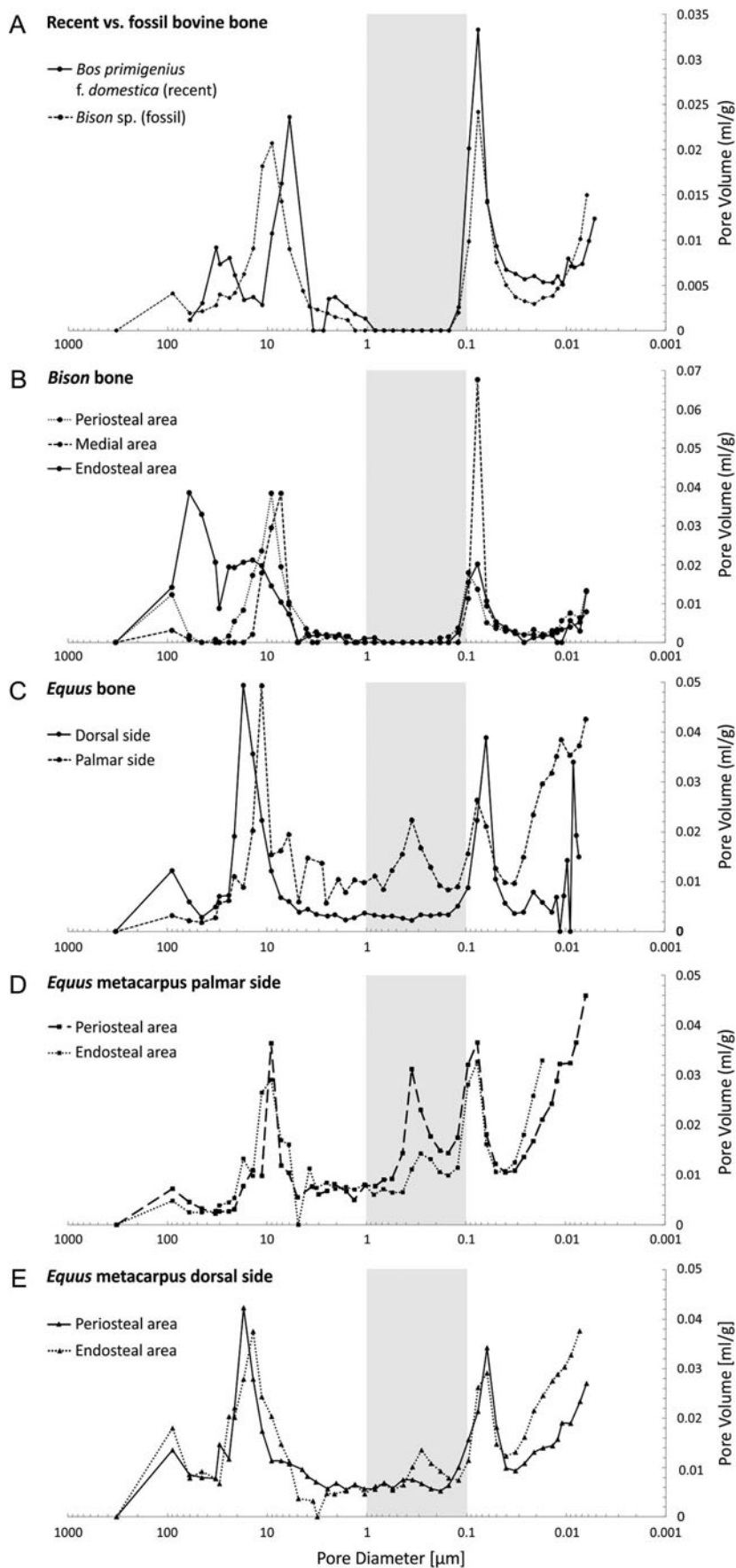


Figure 6. Pore size distributions in the studied cortical tissues. (A) Recent and fossil bovines; (B) periosteal, medial, and endosteal area in fossil bison; (C) the fossil horse; (D) periosteal and endosteal areas of the horse metacarpus palmar side; (E) periosteal and endosteal areas of the horse metacarpus dorsal side. The gray-highlighted areas represent ranges of porosity induced by microbial activity.

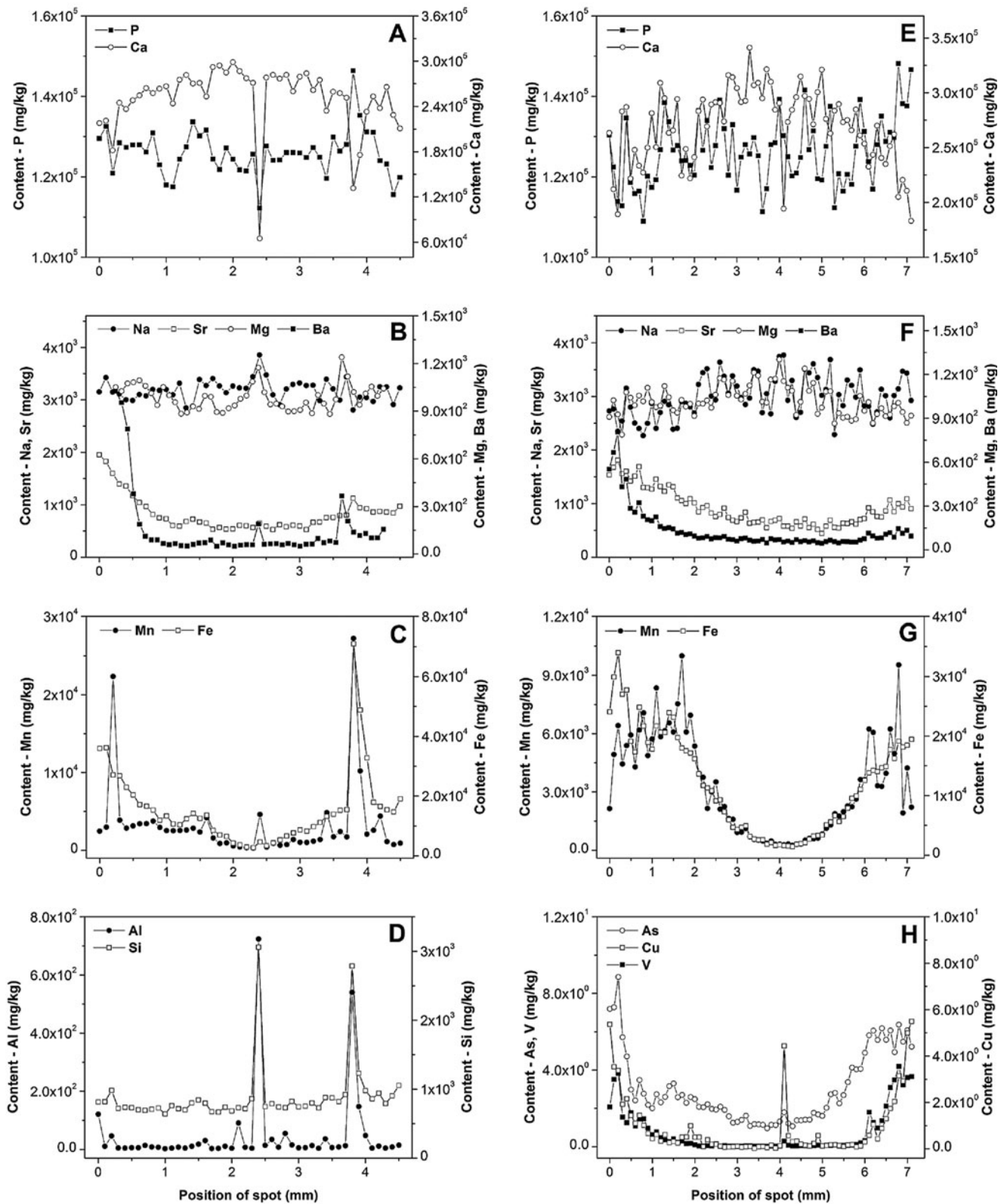


Figure 7. Two-dimensional elemental distribution on the fossil horse bone (BAS) determined by LA-ICP-MS in the spot mode line across the palmar (A–D) and dorsal (E–H) side. The line of spots was situated from periosteum (left) to endosteum (right).

burial in solid permafrost. The differential preservation of the dorsal and palmar sides of the horse bone indicates different mechanisms of recent weathering, with the palmar side buried

in sediments and the dorsal side open-air exposed to multiple freeze-thaw and dry-wet cycles after bone exhumation from the thawing cryolithic deposits of the Batahay thermokarst sinkhole.

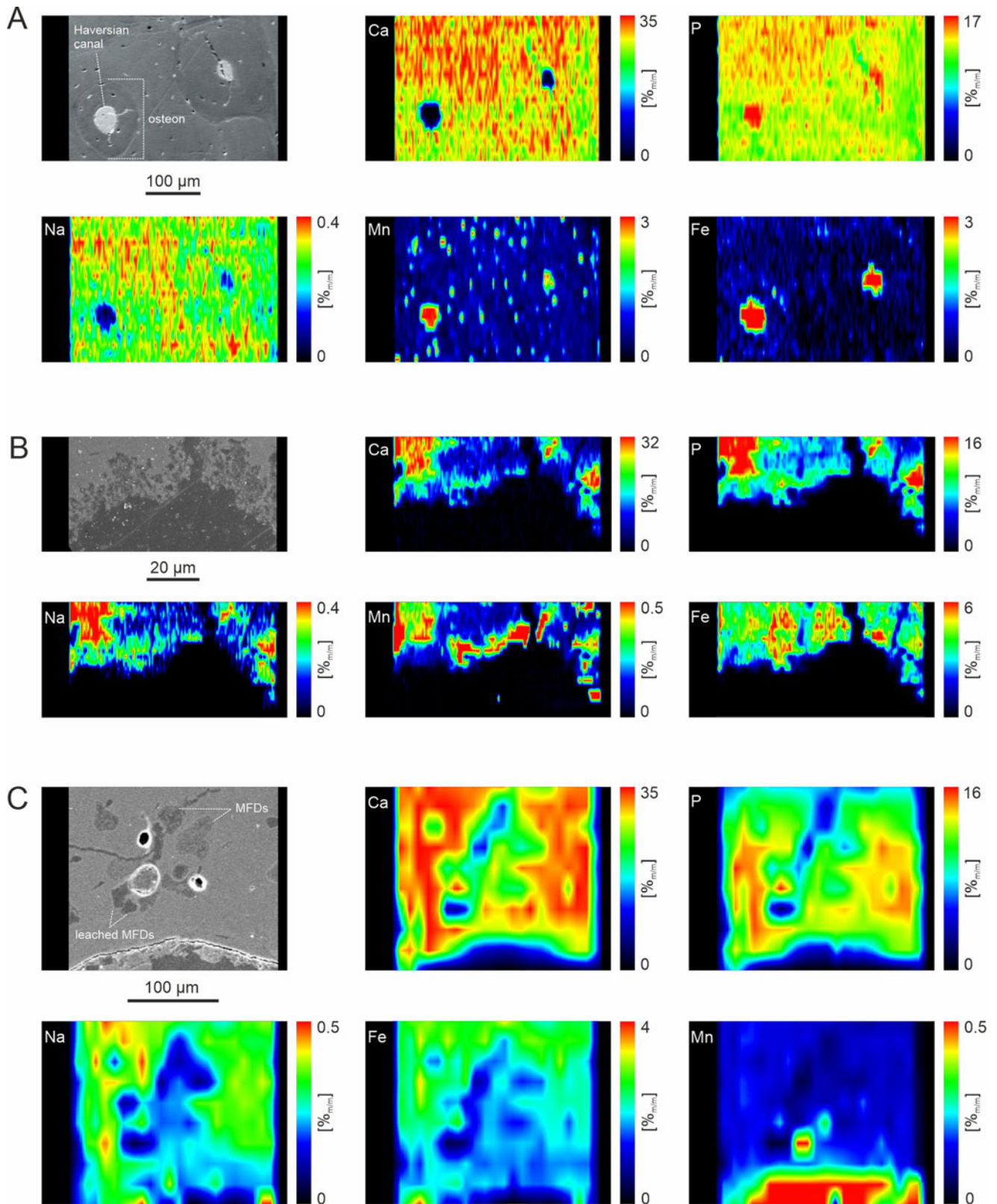


Figure 8. Two-dimensional elemental mapping (LA-ICP-MS analysis) of the fossil horse cortical bone. (A) Images showing vascular canals filled with iron phosphate vivianite; (B) dissolved bone tissue of the secondary osteon with the vascular canal and secondary microporosity in the vicinity filled with manganese-/iron- (oxy) hydroxides in the periosteal bone area; (C) the microbial focal destruction with almost no impurities contrasted with the surrounding bone tissue in the endosteal bone area.

The desiccation process (solar exposure and freezing) due to the extreme seasonal conditions caused loss of moisture from the bone, which generated cracking and flaking (Miller, 1975; Murphy et al., 1981) of the dorsal side of the bone and alteration of its physical properties including decrease of natural biomechanical resistance (Johnson, 1985).

The horse bone was buried under relatively warm/moderate Late Pleistocene climatic conditions and changing ground humidity. This is indicated by increased mobility of humic substances, the presence of Fe-hydroxide coatings on the sealing sand grains, and a dark mineral coloring on the periosteal and the endosteal bone surfaces (Fig. 3B). The prominent longitudinal crack was probably created as a result of shrinkage of collagen fibers during recent desiccation. Hydrolysis of the collagen is reflected by the increase of S-porosity, mainly in the periosteal area of the palmar side (Fig. 6D). However, no massive microcracks have been observed in the horse bone, which is in contrast to (sub-)fossil bones deposited in warm and arid settings (Nacarino-Meneses, 2021) or affected by moisture and temperature fluctuations (Přetřschner and Tütken, 2011; Mayer et al., 2020).

The well-documented MFDs in the *Equus* sample (Figs. 5A–D, 6C, D) show at least two generations of bacterial populations, which must have been controlled by past burial of the bone within the active permafrost layer with periods of increased microbial activity during the summer months of the MIS 3 interstadial and inhibited activity for most of the year. The absence of exogenous elements within the MFDs (Fig. 8C) indicates that bacterial alterations formed before the bone was contaminated with the exogenous elements.

Arctic soils and even the underlying permafrost contain a wide range of bacteria (Nelson and Parkinson, 1978; Shi et al., 1997; Vorobyova et al., 1997; Vishnivetskaya et al., 2001, 2006; Gilichinsky et al., 2008), including gram-positive bacteria (e.g., Firmicutes, Actinobacteria, Cyanobacteria) and gram-negative bacteria (e.g., Alpha-, Beta-, Gamma-Proteobacteria), of which *Bacillus* (gram +) and *Pseudomonas* (gram -) have been described by C.A. Baud (1986) as the most active in postmortem bone attack. Aerobic soil bacteria most probably were involved in the formation of MFDs inside the Yakutian horse bone. The arctic microbial communities are also highly resistant to thawing stress (Gilichinsky et al., 2008).

The presence of exogenous elements inside the fossil bone (Figs. 7, 8; Tables 1–4) shows their increased concentrations in the sealing geological sediments (Lambert et al., 1985). Mineral dissolution mainly in the periosteal area (Fig. 5E, F) most probably resulted from waterlogged and poorly oxygenated conditions that caused chemical hydrolysis of the collagen fibers accompanied by destabilization of bone minerals (Turner-Walker, 2008). The hypermineralized rim shows a high resistance to leaching due to recrystallization of hydroxyapatite, which became larger and more stable due to diagenesis (Hedges, 2002). This is documented by MFD overlapping of chemically altered zones close to the vascular canal (Fig. 5D).

The presence of vivianite in the vascular canals (Figs. 5F, 8A; Table 3) attests to the low-oxygen, periodically or permanently waterlogged, often alkaline conditions (McGowan and Prangnell, 2006; Rothe et al., 2016). The source of hydrogenous iron in the form of Fe³⁺ oxy-hydroxides relates to the sealing sediment. Vivianite precipitation is often mediated by metal-reducing bacteria from the soil (Zachara et al., 1998) in the early stage of bone diagenesis (Turner-Walker, 2012). Vivianite is usually found on the bone surface as a product of bone mineral recrystallization (Berg et al.,

1969; Piepenbrink, 1989; Thali et al., 2011; Turner-Walker, 2012; Papageorgopoulou et al., 2015). Vivianite also may be present inside the bone and tooth (Sekanina, 1937; Johanson, 1976; Turner-Walker, 2012) and in the mummified soft tissues sealed in permafrost (Tessadri, 2000; Pabst et al., 2009; Papageorgopoulou et al., 2015). The low vivianite concentrations found on the dorsal side of the horse bone corroborate the nature of this easily soluble and highly unstable mineral (Rothe et al., 2016) after recent bone exposure and oxidation.

Precipitation of Fe-Mn oxide-hydroxides occurred as a result of burial of the *Equus* bone in the active layer after the formation of the MFDs. The increased content of Fe and Mn in the partially dissolved periosteal margin (Fig. 7C, G) indicates that Fe-Mn oxide-hydroxides precipitation was contemporaneous with the secondary microporosity. It is impossible to distinguish between the porosity induced by microbial activity and porosity caused by abiotic (e.g., chemical) processes solely according to the HgIP. Although mercury porosimetry provided a quality image of the pore size distribution in the bone, this method should be used in combination with SEM to identify properly the factors involved in porosity changes. The extent of bone microbial degradation must be verified by the histology study using other methods (e.g., SEM). The Fe³⁺ oxy-hydroxides most likely were precursors of vivianite, which originated as a result of reaction of the pore-percolating water with metal-reducing bacteria under reduction (anaerobic) depositional conditions. Absence of vivianite on the dorsal side of the *Equus* bone is likely associated with recent bone surface weathering and obliteration of the mineral in environmentally unstable oxygenic (open-air) conditions. The high concentration of Mn²⁺ ions in the endosteal margin (Fig. 8B) indicates precipitation of hydroxides under alkaline conditions (pH ~7) and a later transformation into manganese oxides after open-air exposure from permafrost grounds (Stumm and Morgan, 1996; Morgan, 2005). Freshwater bacteria *Pseudomonas putida* (Villalobos et al., 2006; Bargar et al., 2009) also may have contributed to the observed Mn oxides accompanied by the brown colored FePO₄ on the bone surface. On the other hand, Na and Mg have been leaching out from the bone (Fig. 8A). A similar pattern of Mn, Fe uptake, and Na loss was observed in the bovine bone from a boggy environment (Turner-Walker and Peacock, 2008).

The above exogenous elements affected the bone chemical composition as a result of burial within the active permafrost layer. In periglacial areas, bone microbiota (e.g., fungi, algae, bacteria, and Protozoa) along with chemical degradation strongly depend on ground temperature and water availability (White and Hannus, 1983; Von Endt and Ortner, 1984). The reconstructed MAAT at the Batagay (*Equus*) site during MIS 3 derived from ice-wedges (−35‰ δ¹⁸O) are among the lowest in Yakutia (Opel et al., 2019). Despite extremely cold winters, the summer months were rather warm with high melt water supply (Opel et al., 2019) approaching the present ones recorded in NW Yakutia (Chlachula and Czerniawska, 2021). The interstadial environmental conditions were favorable for incorporation of exogenous elements into the bone structure prior to its complete freezing, as well as soon after its exposure.

The combined analytical multi-proxy evidence of differential preservation of the studied Pleistocene fossils demonstrates a very rapid rate of horse bone structure deterioration shortly after exposure from the permafrost. A range of a few years is assumed to be sufficient for disintegration of an intact bone, following several tens-of-thousands of years of permafrost burial.

CONCLUSIONS

The osteological material of the mid-last glacial (MIS 3) interstadial from the Yana Basin was treated as an example of the diametrically different fossil bone states (compact fresh versus rather weathered bones) of the large Late Pleistocene herbivores *Bison* and *Equus*. The differential preservation of the analyzed fossil remains illustrates the locally specific environmental histories and the post-mortem and post-depositional processes of the fossil fauna records that resulted in the spectrum of bone structure conservation and diagenesis. The applied analytical methods identified several diagenetic factors in the comparative osteological samples. The *Bison* metacarpus remained almost microbiologically intact over the last ca. 45,000 years while frozen in permafrost until its recovery. Only superficial resorption pits with honeycomb pattern, most probably created by aquatic microorganisms, have been observed on the bone surface. On the other hand, the *Equus* metacarpus exposed on the surface during the 2–5 most-recent years shows more extensive bacterial degradation with typical microscopic focal destruction, as well as chemical degradation of the periosteum. The study shows that the application of the HgIP frequently used for estimation of the degree of microbial attack is not reliable if applied separately because other (chemical) processes also can produce pores of a similar diameter (0.1–1 µm). LA-ICP-MS, which detailed the element distribution in the studied bones and within the specific zones on a micrometer scale, helped to detect specific diagenetic events. Along with EMPA, the analyses gave a clearer image of the nature of the depositional and preservational settings.

Fossil fauna remains of diverse physical preservation and chemical composition constitute an informative proxy for reconstruction of past environments, taphonomies of the fossil fauna communities, and the post-mortem processes of particular osteological records. Solid permafrost provides a perfect long-term cryogenic preservation of organic remains, including soft tissue. On the contrary, due to the current extreme climate shifts in North Siberia and the rising MAAT, destruction/degradation of both the ancient and recent skeletal material is rather rapid once the remains are removed from the intact cryogenic grounds. This awareness contributes to the paleontological field reconnaissance in the (sub-)Arctic zone and enhanced understanding of the forms and intensity of the decay of fossil remains.

Acknowledgments. The paleontological investigations in Yakutia were supported by the North-Eastern Federal University, Yakutsk, as a part of the project “Influence of Climate Change to Natural Environments and Peoples in Northern Yakutia” (Jiří Chlachula and Jolanta Czerniawska, 2014). The analytical study was supported by research project MUNI/1263/2020 of the Faculty of Science at the Masaryk University in Brno, Czech Republic (Martin Ivanov); the Ministry of Culture of the Czech Republic within the development program MK000094862 and the Moravian Museum Brno (Gabriela Calábková); the Student Project Grant MUNI/A/1390/2020 of Masaryk University (Michaela Hložková); and the projects FCH-S-21-7398 of the Czech Ministry of Education, Youth and Sports (Michaela Vašínová Galiová). Jindřich Kynický (BIC Brno) provided funding for the LA-ICP analysis. Kyunnei Pestereeva (Laboratory of Archaeology, the North-Eastern Federal University, Yakutsk) assisted in the Yana region field investigations. The authors thank two anonymous reviewers for their very constructive comments and views that improved the original manuscript.

REFERENCES

Agroclimate Database, 1963. *Agroclimate Base of the Yakutian SSR*. Gidrometeozdat, Leningrad, 145 p. [in Russian]

- Andreev, A.A., Klimanov, V.A., Sulerzhitsky, L.D.**, 2001. Vegetation and climate history of the Yana River lowland, Russia, during the last 6400 yr. *Quaternary Science Reviews* **20**, 259–266.
- Ashastina, K., Kuzmina, S., Rudaya, N., Troeva-Werner, E., Schock, H., Roemermann, C., Reineck, J., et al.**, 2018. Woodlands and steppes: Pleistocene vegetation in Yakutia’s most continental part recorded in the Batagay permafrost sequence. *Quaternary Science Reviews* **196**, 38–61.
- Bargar, J.R., Fuller, C.C., Marcus, M.A., Brearley, A.J., De la Rosa, M.P., Webb, S.M., Caldwell, W.A.**, 2009. Structural characterization of terrestrial microbial Mn oxides from Pinal creek, AZ. *Geochimica et Cosmochimica Acta* **73**, 889–910.
- Baud, C.-A.**, 1986. Altérations osseuse post-mortem d’origine fongique ou bactérienne. In: Duday, H., Masset, C. (Eds.), *Anthropologie Physique et Archéologie: Méthodes d’Étude des Sépultures*. CNRS, Paris, pp. 135–146.
- Behrensmeyer, A.K.**, 1978. Taphonomic and ecologic information from bone weathering. *Paleobiology* **4**, 150–162.
- Bell, L.S., Skinner, M.F., Jones, S.J.**, 1996. The speed of post mortem change to the human skeleton and its taphonomic significance. *Forensic Science International* **82**, 129–140.
- Berg, S., Doring, G., Suchenwirth, H., Weiner, K.L.**, 1969. Beobachtungen über das Verhalten von Fettwachsleichen in grösserer Wassertiefe. *Archiv für Kriminologie* **143**, 148–162.
- Berna, F., Matthews, A., Weiner, S.**, 2004. Solubilities of bone mineral from archaeological sites: the recrystallization window. *Journal of Archaeological Science* **31**, 867–882.
- Binford, L.R.**, 1978. *Nunamiut Ethnoarchaeology*. Academic Press, New York, 509 pp.
- Biske, S.F.**, 1957. Quaternary deposits of the Kolyma Lowland. In: *Materials on Geology and Mineral Resources of Northeast USSR*. Magadan Publishing House, Magadan, USSR, v. 2, pp. 68–81. [in Russian]
- Boeskorov, G.G.**, 2005. *Formation of the Present Territory of Yakutia (Late Pleistocene–Holocene)*. PhD Dissertation, Yakutsk, Russia, North-Eastern Federal University, 339 pp. [in Russian]
- Boeskorov, G.G.**, 2009. Preliminary data on the find of a mummified body of woolly rhinoceros find in the lower reaches of the Kolyma Basin. *Doklady RAN* **424**, 570–573. [in Russian]
- Boeskorov, G.G.**, 2010. *Catalogue of Osteological Collection of the Yakutsk State Museum of History and Culture of the Northern Nations*. Dani Almas Press, Yakutsk, Russia, v. 2, 70 pp. [in Russian]
- Boeskorov, G.G., Protopopov A.V., Mashchenko, E.N.**, 2013. New occurrences of fossil mammals of unique preservation in the permafrost of Yakutia. *Zoological Journal* **452**, 461–465.
- Bulygina, O.N., Razuvaev, V.N.**, 2012. *Daily Temperature and Precipitation Data for 518 Russian Meteorological Stations (1881–2010)*. Carbon Dioxide Information Analysis Center. Oak Ridge National Laboratory. U.S. Department of Energy, Oak Ridge, Tennessee. <https://doi.org/10.3334/CDIAC/cli.100>.
- Byrd, J.H., Castner, J.L.**, 2010. *Forensic Entomology: The Utility of Arthropods in Legal Investigations, 2nd ed.* CRC Press, Boca Raton, Florida, 705 pp.
- Carter, D.O., Yellowlees, D., Tibbett, M.**, 2007. Cadaver decomposition in terrestrial ecosystems. *Naturwissenschaften* **94**, 12–24
- Cowin, S.C.**, 1999. Bone poroelasticity. *Journal of Biomechanics* **32**, 217–238.
- Cheprasov, M.Yu., Obada, T.F., Grigoriev, S.E., Novgorodov, G.P., Marareskul, V.A.**, 2015. New locations of the mammoth fauna and Palaeolithic sites in the basin of the Kolyma River. *Vestnik of the North-Eastern Federal University Yakutsk* **6**, 53–68. [in Russian]
- Chernova, O.E., Kirillova, L.V., Boeskorov, G.G., Shidlovskiy, F.K., Kabilov, M.R.**, 2015. Architectonics of the hairs of the woolly mammoth and woolly rhino. *Proceedings of the Geological Institute RAS* **319**, 441–460.
- Chlachula, J., Czerniawska, J.**, 2021. Geo-environmental response to present climate warming in Subarctic East Siberia. Abstract Book, PaleoArc 2021, 2nd International Conference on Processes and Paleo-environmental Changes in the Arctic from Past to Present, Pisa, Italy, 24–25 May 2021, p. 26.
- Chlachula, J., Czerniawska, J., Pestereva, K., Pesterev, D.**, 2014. Geological and environmental contexts of Pleistocene occupation of the central Yana River basin, northern Yakutia. Eurasia in Cenozoic: *Stratigraphy, Palaeoecology, Culture* **3**, 166–175.
- Chlachula, J., Cheprasov, M.Yu., Novgorodov, G.P., Obada, T., Little, E.**, 2021. The Late Pleistocene–Early Holocene environments of the Kolyma

- Basin: implications for the Palaeolithic occupation of NE Siberia. *Boreas* **50**, 556–581.
- Chukanov, N.V., Scholz, R., Zubkova, N.V., Pekov, I.V., Belakovskiy, D.I., Van, K.V., Lagoeiro, L., et al., 2014. Corraínevesite, $\text{Fe}^{2+}\text{Mn}^{2+}(\text{PO}_4)_2 \cdot 3\text{H}_2\text{O}$, a new reddingite-group mineral from the Cigana mine, Conselheiro Pena, Minas Gerais, Brazil. *American Mineralogist*, **99**, 811–816.
- Czerniawska, J., Chlachula, J., 2020. Climate-change induced permafrost degradation in Yakutia. *Arctic* **73**, 509–528.
- Danilov, Y.G., Degteva, Z.F., 2018. Modern dynamics of climate change eastern economic zone of Yakutia. *Vestnik NEFU Yakutsk (Earth Sciences Series)* **2**, 41–56. [in Russian]
- Davis, P.G., 1997. The bioerosion of bird bones. *International Journal of Osteoarchaeology* **7**, 388–401.
- de Sousa, D.V., Eltink, E., Oliveira, R.A.P., Félix, J.F., Guimarães, L.M., 2020. Diagenetic processes in Quaternary fossil bones from tropical limestone caves. *Scientific Reports* **10**, 21425. <https://doi.org/10.1038/s41598-020-78482-0>.
- Duchkov, A., 2006. Characteristics of permafrost in Siberia. In: Lombardi S., Altunina L., Beaubien S. (Eds.), *Advances in the Geological Storage of Carbon Dioxide*. NATO Science Series: IV: Earth and Environmental Sciences. Springer, Dordrecht, 65. https://doi.org/10.1007/1-4020-4471-2_08.
- Erzincioğlu, Z., 1996. *Blowflies*. Naturalists' Handbooks 23, Richmond Publishing Co. Ltd, Slough, UK.
- Fedorov, A.N., Gavriliev, P.P., Konstantinov, P.Y., Hiyama, T., Iijima, Y., Iwahana, G., 2014. Estimating the water balance of a thermokarst lake in the middle of the Lena River basin, eastern Siberia. *Eco-hydrology* **7**, 188–196.
- Fedorov, A.N., Vasilyev, N.F., Torgovkin, Y.I., Shestakova, A.A., Varlamov, S.P., Zheleznyak, M.N., Shepelev, V.V., et al., 2018. Permafrost-landscape map of the Republic of Sakha (Yakutia) on a scale 1:1,500,000. *Geosciences* **8**, 465. <https://doi.org/10.3390/geosciences8120465>.
- Fernández-Jalvo, Y., Andrews, P., 2016. *Atlas of Taphonomic Identifications: 1001+ Images of Fossil and Recent Mammal Bone Modification*. Springer, Dordrecht, Germany, 359 pp.
- Fernández-Jalvo, Y., Andrews, P., Pesquero, D., Smith, C., Marín-Monfort, D., Sánchez, B., Geigl, E.M., Alonso, A., 2010. Early bone diagenesis in temperate environments Part I: Surface features and histology. *Palaeogeography, Palaeoclimatology, Palaeoecology* **288**, 62–81.
- Frenzel, B., 1962. Maximum cooling of the last glaciation (about 20,000 to 18,000 years BP), in: Frenzel, B., Péczli, M., Velichko, A.A. (Eds.), *Atlas of Paleoclimates and Paleoenvironments of the Northern Hemisphere, Late Pleistocene Holocene*. Geographical Institute, Hungarian Academy of Sciences and Gustav Fisher Verlag, Budapest, Stuttgart, pp. 97–99.
- Galiova, M., Kaiser, J., Fortes, F.J., Novotny, K., Malina, R., Prokes, L., Hrdlicka, A., et al., 2010. Multielemental analysis of prehistoric animal teeth by laser-induced breakdown spectroscopy and laser ablation inductively coupled plasma mass spectrometry. *Applied Optics* **49**, 191–199.
- Gilchinsky, D., Vishnivetskaya, T., Petrova, M., Spirina, E., Mamykin, V., Rivkina, E., 2008. Bacteria in permafrost. In: Margesin, R., Schinner, F., Marx, J.C., Gerday, C. (Eds.), *Psychrophiles: From Biodiversity to Biotechnology*. Springer, Berlin, Heidelberg, pp. 83–102.
- Goodwin, M.B., Grant, P.G., Bench, G., Holroyd, P.A., 2007. Elemental composition and diagenetic alteration of dinosaur bone: distinguishing micron-scale spatial and compositional heterogeneity using PIXE. *Palaeogeography, Palaeoclimatology, Palaeoecology* **253**, 458–476.
- Grassberger, M., Reiter, C., 2002. Effect of temperature on development of the forensically important holarctic blow fly *Protophormia terraenovae* (Robineau-Desvoidy) (Diptera: Calliphoridae). *Forensic Science International* **128**, 3, 177–182.
- Grose, G., Robinson, J.E., Bryant, R., Taylor, M.D., Veremeeva, A., Schirmer, L., Harde, J., 2013. Distribution of Late Pleistocene ice-rich syngenetic permafrost of the Yedoma suite in East and Central Siberia, Russia. *U.S. Geological Survey Open-File Report* 1078, 37 pp.
- Hackett, C.J., 1981. Microscopical focal destruction (tunnels) in exhumed human bones. *Medicine, Science and the Law* **21**, 243–265.
- Harada, K., Wada, K., Sueyoshi, T., Fukuda, M., 2006. Resistivity structures in alar areas in Central Yakutia, Siberia, and the interpretation of permafrost history. *Permafrost and Periglacial Processes* **17**, 105–118.
- Hedges, R.E.M., 2002. Bone diagenesis: an overview of processes. *Archeometry* **44**, 319–328.
- Iijima, Y., Fedorov, A.N., Park, H., Suzuki, K., Yabuki, H., Maximov, T.C., Ohata, T., 2010. Abrupt increases in soil temperatures following increased precipitation in a permafrost region, central Lena River basin, Russia. *Permafrost and Periglacial Processes* **21**, 30–41.
- Jacks, M., Sherburne, R., Lubbel, D., Barker, C., Wayman, M., 2001. Destruction of microstructure in archaeological bone: a case study from Portugal. *International Journal of Osteoarchaeology* **11**, 415–432.
- Janaway, R.C., Percival, S.L., Wilson, A.S., 2009. Decomposition of human remains. In: Percival, S.L. (Ed.), *Microbiology and Aging*. The Humana Press, New York, pp. 313–334.
- Jans, M.M.E., 2008. Microbial bioerosion of bone—a review. In: Wisshak, M., Tapanila, L. (Eds.), *Current Developments in Bioerosion*. Erlangen Earth Conference Series, Springer-Verlag, Berlin, pp. 397–414.
- Jans, M.M.E., Nielsen-Marsh, C.M., Smith, C.I., Collins, M.J., Kars, H., 2004. Characterisation of microbial attack on archaeological bone. *Journal of Archaeological Science* **31**, 87–95.
- Johanson, G., 1976. Iron from cannon balls in teeth and jaws. *Ossa*, **3–4**, 183–187.
- Johnson, E., 1985. Current developments in bone technology. *Advances in Archaeological Method and Theory* **8**, 157–235.
- Keenan, S.W., Engel, A.S., 2017. Early diagenesis and recrystallization of bone. *Geochimica et Cosmochimica Acta* **196**, 209–223.
- Kendall, C., Eriksen, A.M.H., Kontopoulos, I., Collins, M.J., Turner-Walker, G., 2018. Diagenesis of archaeological bone and tooth. *Palaeogeography, Palaeoclimatology, Palaeoecology* **491**, 21–37.
- Kirillova, I.V., Borisova, O.K., Chernova, O.F., van Kolschoten, T., van der Lubbe, J.H.I., Panin, A.V., Pečňerová, P., et al., 2020. 'Semi-dwarf' woolly mammoths from the East Siberian Sea coast, continental Russia. *Boreas* **49**, 269–285.
- Kremer, B., Owocki, K., Królikowska, A., Wrzosek, B., Kazmierczak, J., 2012. Mineral microbial structures in a bone of the Late Cretaceous dinosaur *Sauroplophus angustirostris* from the Gobi Desert, Mongolia—a Raman spectroscopy study. *Palaeogeography, Palaeoclimatology, Palaeoecology* **358–360**, 51–61.
- Kunitsky, V.V., Syromyatnikov, I.I., Schirmer, L., Skachkov, Yu.B., Grosse, G., Wetterich, S., Grigoriev, M.N., 2013. Ice-rich permafrost and thermal denudation in the Batagay area (Yana Upland, East Siberia). *Earth Cryosphere [Kriosfera Zemli]* **17**, 56–68. [in Russian]
- Lambert, J.B., Simpson, S.V., Weiner, S.G., Buikstra, J.E., 1985. Induced metal-ion exchange in excavated human bone. *Journal of Archaeological Science* **12**, 85–92.
- Lazarev, P.A., 2008. *Large Mammals of Anthropogene of Yakutia*. Nauka, Novosibirsk, 169 pp.
- Lazarev, P.A., Grigor'ev, S.E., Plotnikov, V.V., Savvinov, G.N., 2011. Findings of unique remains of horse and bison in the Verkhoyansk Region of Yakutia. *Problems of Regional Ecology* **4**, 13–18. [In Russian]
- Lebon, M., Reiche, I., Bahain, J.J., Chadeaux, C., Moigne, A.M., Frohlich, F., Semah, F., Schwarcz, H.P., Falgueres, C., 2010. New parameters for the characterization of diagenetic alterations and heat-induced changes of fossil bone mineral using Fourier transform infrared spectrometry. *Journal of Archaeological Science* **37**, 2265–2276.
- Legros, R., Balmain, N., Bonel, G., 1987. Age-related changes in mineral of rat and bovine cortical bone. *Calcified Tissue International* **41**, 137–144.
- Liao, J.L., Sun, X.M., Li, D.F., Sa, R.N., Lu, Y., Lin, Z.Y., Xu, L., Zhan, R.Z., Pan, Y.G., Xu, H.F., 2019. New insights into nanostructure and geochemistry of bioapatite in REE-rich deep-sea sediments: LA-ICP-MS, TEM, and Z-contrast imaging studies. *Chemical Geology* **512**, 58–68.
- Malkova, G.V., Pavlov, A.V., Skachkov, Yu.B., 2011. Assessment of permafrost stability under contemporary climatic change. *Earth's Cryosphere* **15**, 4, 29–32.
- Mandernack, K.W., Post, J., Tebo, B.M., 1995a. Manganese mineral formation by bacterial spores of the marine *Bacillus* sp. Strain SG-1: evidence for the direct oxidation of Mn(II) to Mn(IV). *Geochimica et Cosmochimica Acta* **59**, 4393–4408.
- Mandernack, K.W., Fogel, M.L., Tebo, B.M., Usui, A., 1995b. Oxygen isotope analyses of chemically and microbially produced manganese oxides and manganates. *Geochimica et Cosmochimica Acta* **59**, 4409–4425.

- Marchifava, V., Bonucci, E., Ascenzi, A., 1974. Fungal osteoclasia: a model of dead bone resorption. *Calcified Tissue Research* **14**, 195–210.
- Mayer, E.L., Hubbe, A., Botha-Brink, J., Ribeiro, A.M., Haddad-Martim, P.M., Neves, W., 2020. Diagenetic changes on bone histology of Quaternary mammals from a tropical cave deposit in southeastern Brazil. *Palaeogeography, Palaeoclimatology, Palaeoecology* **537**, 109372. <https://doi.org/10.1016/j.palaeo.2019.109372>.
- McGowan, G., Prangnell, J., 2006. The significance of vivianite in archaeological settings. *Geoarchaeology* **21**, 93–111.
- Merlet, C., 1994. An accurate computer correction program for quantitative electron probe microanalysis. *Mikrochimica Acta* **114/115**, 363–376.
- Micozzi, M.S., 1997. Frozen environments and soft tissue preservation. In: Haglund, W.D., Sorg, M.H. (Eds.), *Forensic Taphonomy: The Postmortem Fate of Human Remains*. CRC Press, Boca Raton, Florida, pp. 171–180.
- Miller, G.J., 1975. A study of cuts, grooves and other marks on recent fossil bone: II. Weathering cracks, fractures, splinters, and other similar natural phenomena. In: Swanson, E. (Ed.), *Lithic Technology: Making and Using Stone Tools*. Mouton, The Hague, pp. 211–226.
- Morgan, J.J., 2005. Kinetics of reaction between O₂ and Mn(II) species in aqueous solutions. *Geochimica et Cosmochimica Acta* **69**, 35–48.
- Murphy, L., Barnett, B.G., Holloway, R.G., Sheldon, C.M., 1981. An experiment to determine the effects of wet/dry cycling on certain common cultural materials. In: Lenihan, D.J., Carrell, T.L., Fosberg, S., Murphy, L., Rayl, S.L., and Ware, J.A. (Eds.), *The Final Report of the National Reservoir Inundation Study*. Technical Report 8-1-8-43. Sante Fe, New Mexico: USDI, National Park Service, Southwest Cultural Resources Center, v. 2.
- Murton, J.B., Edwards, M.E., Lozhkin, A.V., Anderson, P.M., Savvinov, G.N., Bakulina, N., Bondarenko, O.V., et al., 2017. Preliminary paleoenvironmental analysis of permafrost deposits at Batagaika megaslump, Yana Uplands, northeast Siberia. *Quaternary Research* **87**, 314–330.
- Müller, K., Chadeaux, C., Thomas, N., Rieche, I., 2011. Microbial attack of archaeological bones versus high concentrations of heavy metals in the burial environment. A case study of animal bones from a mediaeval copper workshop in Paris. *Palaeogeography, Palaeoclimatology, Palaeoecology* **310**, 39–51.
- Nacarino-Meneses, C., Chinsamy, A., Mayda, S., Kaya, T., Erisimis, U., 2021. Bone histology, palaeobiology, and early diagenetic history of extinct equids from Turkey. *Quaternary Research* **100**, 240–259.
- Nelson, L.M., Parkinson, D., 1978. Growth characteristics of three bacterial isolates from an arctic soil. *Canadian Journal of Microbiology* **24**, 909–914.
- Opel, T., Murton, J.B., Wetterich, S., Meyer, H., Ashastina, K., Günther, F., Grotheer, H., et al., 2019. Past climate and continentality inferred from ice wedges at Batagay megaslump in the Northern Hemisphere's most continental region, Yana Highlands, interior Yakutia. *Climate of the Past* **15**, 1443–1461.
- Pabst, M.A., Letofsky-Papst, I., Bock, E., Moser, M., Dorfer, L., Egarter-Vigl, E., Hofe, F., 2009. The tattoos of the Tyrolean Iceman: a light microscopical, ultrastructural and element analytical study. *Journal of Archaeological Science* **36**, 2335–2341.
- Papageorgopoulou, Ch., Link, K., Ruhli F. J., 2015. Histology of a woolly mammoth (*Mammuthus primigenius*) preserved in permafrost, Yamal Peninsula, Northwest Siberia. *The Anatomical Record* **298**, 1059–1071.
- Pfretzschner, H.U., Tütken, T., 2011. Rolling bones—taphonomy of Jurassic dinosaur bones inferred from diagenetic microcracks and mineral infillings. *Palaeogeography, Palaeoclimatology, Palaeoecology* **310**, 117–123.
- Piepenbrink, H., 1989. Examples of chemical changes during fossilization. *Applied Geochemistry* **4**, 273–280.
- Piga, G., Santos-Cubedo, A., Sola, S.M., Brunetti, A., Malgosa, A., Enzo, S., 2009. An X-ray Diffraction (XRD) and X-ray Fluorescence (XRF) investigation in human and animal fossil bones from Holocene to Middle Triassic. *Journal of Archaeological Science* **36**, 1857–1868.
- Plotnikov, V.V., Protopopov, A.V., Kolesov, S.D., Klimovskiy, A.I., 2016. Overview and preliminary analysis of the new finds of woolly mammoth (*Mammuthus primigenius* Blumenbach, 1799) in the Yana-Indigirka lowland, Yakutia, Russia. *Quaternary International* **406**, 70–85.
- Popp, S., Diekmann, B., Meyer, H., Siegert, C., Syromiatnikov, I., Hubberten, H.S., 2006. Palaeoclimate signals as inferred from stable-isotope composition of ground ice in the Verkhoyansk Foreland, Central Yakutia. *Permafrost and Periglacial Processes* **17**, 119–132.
- Pratesi, G., Cipriani, C., Giuli, G., Birch, W.D., 2003. Santabarbarite: a new amorphous phosphate mineral. *European Journal of Mineralogy* **15**, 185–192.
- Relucanti M., Miglietta S., Bove G., Donfrancesco O., Battaglione E., Familiari P., Barbaranelli C., Covelli E., Barbara M., Familiari G., 2020. SEM BSE 3D image analysis of human incus bone affected by cholesteatoma ascribes to osteoclasts the bone erosion and VpSEM dEDX analysis reveals new bone formation. *Hindawi* 2020, 9371516. <https://doi.org/10.1155/2020/9371516>.
- Reynard, B., Balter, V., 2014. Trace elements and their isotopes in bones and teeth: diet, environments, diagenesis, and dating of archeological and paleontological samples. *Palaeogeography, Palaeoclimatology, Palaeoecology* **416**, 4–16.
- Romanovsky, V.E., Drozdov, D.S., Oberman, N.G., Malkova, G.V., Kholodov, A.L., Marchenko, S.S., Moskalenko, N.G., et al., 2010. Thermal state of permafrost in Russia. *Permafrost and Periglacial Processes* **21**, 136–155.
- Rothe, M., Kleeberg, A., Hupfer, M., 2016. The occurrence, identification and environmental relevance of vivianite in waterlogged soils and aquatic sediments. *Earth-Science Reviews* **158**, 51–64.
- Schuur, E.A.G., McGuire, A.D., Schadel, C., Grosse, G., Harden, J.W., Hayes, D.J., Hugelius, G., et al., 2015. Climate change and the permafrost carbon feedback. *Nature* **520**, 171–179.
- Sekanina, J., 1937. Über zwei neue Phosphatvorkommen in Mähren (Nové Nálezy Fosforecnanů na Moravě). Píspvy vydávané Přírodovědeckou fakultou Masarykovy University 231, Knihkupectví A. Písa, Brno, Česká.
- Shi, T., Reeves, R.H., Gilichinsky, D.A., Friedmann, E.I., 1997. Characterization of viable bacteria from Siberian permafrost by 16S rDNA sequencing. *Microbial Ecology* **33**, 169–179.
- Sillen, A., Parkington, J., 1996. Diagenesis of bones from Eland's Bay Cave. *Journal of Archaeological Science* **23**, 535–542.
- Skinner, H.C.W., 2005. Mineralogy of bone. In: Selinus, O. (Ed.), *Essentials of Medical Geology. Impact of the Natural Environment on Public Health*. Elsevier, Amsterdam, pp. 667–693.
- Smith, K.G.V., 1986. *A Manual of Forensic Entomology*. Cornell University Press, Ithaca, NY.
- Stumm, W., Morgan, J.J., 1996. *Aquatic Chemistry: Chemical Equilibria and Rates in Natural Waters*. John Wiley and Sons, New York, 1022 p.
- Sutcliffe, A.J., 1990. Rates of decay of mammalian remains in the permafrost environment of the Canadian High Arctic. In: Harington, C.R. (Ed.), *Canada's Missing Dimension: Science and History in the Canadian Arctic Islands*. Canadian Museum of Nature, Ottawa, v. 1, pp. 161–186.
- Swanston, T., Varney, T., Coulthard, I., Feng, R.F., Bewer, B., Murphy, R., Hennig, C., Cooper, D., 2012. Element localization in archaeological bone using synchrotron radiation X-ray fluorescence: identification of biogenic uptake. *Journal of Archaeological Science* **39**, 2409–2413.
- Tessadri, R., 2000. Vivianite from the iceman of the Tisenjoch (Tyrol, Austria): mineralogical–chemical data. In: Bortenschlager, S., Oegg, K. (Eds.), *The Iceman and His Natural Environment. The Man in the Ice 4*. https://doi.org/10.1007/978-3-7091-6758-8_11.
- Thali, M.J., Lux, B., Lösch, S., Rösing, F.W., Hurlimann, J., Feer, P., Dirnhofer, R., Königsdorfer, U., Zollinger, U., 2011. “Brienzi”—the blue vivianite man of Switzerland: time since death estimation of an adipocere body. *Forensic Science International* **21**, 34–40.
- Todisco, D., Monchot, H., 2008. Bone weathering in a periglacial environment: the Tayara Site (KbFk-7), Qikirtaq Island, Nunavik (Canada). *Arctic* **61**, 1, 87–101.
- Trueman, C.N.G., Martill, D.M., 2002. The long-term survival of bone: the role of bioerosion. *Archaeometry* **44**, 371–382.
- Turner-Walker, G., 1998. Pyrite and bone diagenesis in terrestrial sediments: evidence from the West Runton Freshwater Bed. *Bulletin of the Geological Society of Norfolk* **48**, 3–26.
- Turner-Walker, G., 2008. The chemical and microbial degradation of bones and teeth. In: Pinhasi, R., Mays, S. (Eds.), *Advances in Human Palaeopathology*. John Wiley & Sons, New York, pp. 3–29.
- Turner-Walker, G., 2012. Early bioerosion in skeletal tissues: persistence through deep time. *Neues Jahrbuch für Geologie und Paläontologie Abhandlungen* **265**, 165–183.

- Turner-Walker, G., 2019. Light at the end of the tunnels? The origins of microbial bioerosion in mineralised collagen. *Palaeogeography, Palaeoclimatology, Palaeoecology* **529**, 24–38.
- Turner-Walker, G., Jans, M.M.E., 2008. Reconstructing taphonomic histories using histological analysis. *Palaeogeography, Palaeoclimatology, Palaeoecology* **266**, 207–235.
- Turner-Walker, G., Peacock, E.E., 2008. Preliminary results of bone diagenesis in Scandinavian bogs. *Palaeogeography, Palaeoclimatology, Palaeoecology* **266**, 151–159.
- Turner-Walker, G., Nielsen-Marsh, C.M., Syversen, U., Kars, H., Collins, M.J., 2002. Sub-micron spongiform porosity is the major ultra-structural alteration occurring in archaeological bone. *International Journal of Osteoarchaeology* **12**, 407–414.
- Vasil'chuk, Yu.K., Vasil'chuk, J.Yu., 2019. The first AMS dating of organic micro-inclusions in an ice wedge. *Doklady AS RAS (Earth Science)* **489**, 1318–1321.
- Velichko, A.A., 1993. *Evolution of Landscapes and Climates of Northern Eurasia, Late Pleistocene–Holocene, Elements of Prognosis. 1. Regional Palaeogeography*. RAN, Institute of Geography, Nauka, Moscow.
- Veremeeva, A.A., Glushkova, N.V., 2013. Spatial regularities of ice-complex thawing in the Holocene in the Kolyma Lowland tundra zone (northern Yakutia). Proceedings, VIIIth All Russian Conference on Quaternary Research, Rostov-on-Don, 10–15 June, 2013, SSC RAS Publishers, Rostov-on-Don, pp. 104–106. [in Russian]
- Villalobos, M., Lanson, B., Manceau, A., Toner, B., Sposito, G., 2006. Structural model for the biogenic Mn oxide produced by *Pseudomonas putida*. *American Mineralogist* **91**, 489–502.
- Vishnivetskaya, T.A., Erokhina, L.G., Spirina, E.V., Shatilovich, A.V., Vorobyova, E.A., Gilichinsky, D.A., 2001. Ancient viable phototrophs within the permafrost. *Nova Hedwigia* **123**, 427–442.
- Vishnivetskaya, T.A., Petrova, M.A., Urbance, J., Ponder, M., Moyer, C.L., Gilichinsky, D.A., Tiedje, J.M., 2006. Bacterial community in ancient Siberian permafrost as characterized by culture and culture-independent methods. *Astrobiology* **6**, 400–414.
- Von Endt, D., Ortner, D., 1984. Experimental effects of bone size and temperature on bone diagenesis. *Journal of Archaeological Science* **11**, 247–253.
- Vorobyova, E., Soina, V., Gorlenko, M., Minkovskaya, N., Zalinova, N., Mamukelashvili, A., Gilichinsky, D., Rivkina, E., Vishnivetskaya, T., 1997. The deep cold biosphere: facts and hypothesis. *FEMS Microbiology Reviews* **20**, 277–290.
- Wedl, C., 1864. Über einen im Zahnbein und Knochen keimenden Pilz. *Akademie der Wissenschaften, Mathematisch-Naturwissenschaftliche Classe, Vienna* **50**, 171–193.
- White, E.M., Hannus, L.A., 1983. Chemical weathering of bone in archaeological soils. *American Antiquity* **48**, 316–322.
- White, L., Booth, T.J., 2014. The origin of bacteria responsible for bioerosion to the internal bone microstructure: results from experimentally-deposited pig carcasses. *Forensic Science International* **239**, 92–102.
- Zachara, J., Fredrickson, J., Li, S., Kennedy, D., Smith, S., Glassman, P., 1998. Bacterial reduction of crystalline Fe³⁺ oxides in single-phase suspensions and subsurface materials. *American Mineralogist* **83**, 1426–1443.